The polarization of microglia and infiltrated macrophages in the injured mice spinal cords: A dynamic analysis

Jing-Lu Li [1, 2], **Gui-Qiang Fu** [1, 2], **Yang-Yang Wang** [1, 2], **Ming-Ming Bian** [1, 2], **Yao-Mei Xu** [1, 2], **Lin Zhang** [1, 2], **Yu-Qing Chen** [1, 2], **Nan Zhang** [1, 2], **Shu-Qin Ding** [1, 2], **Rui Wang** [2], **Rui Fang** [3], **Jie Tang** [2], **Jian-Guo Hu** [1, 2], **He-Zuo Lü** [Corresp. 1, 2]

[1] Clinical Laboratory, the First Affiliated Hospital of Bengbu Medical College, Bengbu, China

[2] Anhui Key Laboratory of Tissue Transplantation, the First Affiliated Hospital of Bengbu Medical College, Bengbu, China

[3] Department of Clinical Medical, Bengbu Medical College, Bengbu, China

Corresponding Author: He-Zuo Lü
Email address: lhz233003@163.com

Background. Following spinal cord injury (SCI), a large number of peripheral monocytes infiltrate into the injured area and differentiate into macrophages (Mø). These monocyte-derived Mø are very difficult to distinguish from the local activated microglia (MG). Therefore, the term Mø/MG are often used to define the infiltrated Mø and/or activated MG. It has been recognized that pro-inflammatory M1-type Mø/MG play "bad guy" roles in the pathological mechanism of SCI. Our recent research showed that in sub-acute spinal cord injured mice local M1 cells are mainly $CD11b^{+}CD45^{-/low}CD68^{+}$. Therefore, we speculated that the M1 cells in the injured spinal cords mainly derived from MG rather than infiltrating Mø. And so far, their dynamics after SCI are not completely clear. **Methods.** Using an Infinite Horizon impactor, the female BALB/c mouse SCI model was made by using a 1.3 mm diameter rod and a 50 Kdynes force. Sham-operated (sham) mice only received a laminectomy without contusive injury. Fow cytometry and immunohistofluorescence were combined to analyze the dynamic changes of polarized Mø and MG in the acute (1 day), subacute (3, 7 and 14 days) and chronic (21 and 28 days) phases of SCI. **Results.** The total Mø/MG gradually increased and peaked at 7 days post-injury (dpi), and maintained at high levels 14, 21 and 28 dpi. Most of the Mø/MG were activated, and the Mø increased significantly at 1 and 3 dpi. However, with the pathological process, the activated MG increased nearly to 90% at 7, 14, 21 and 28 dpi. Both M1 and M2 Mø were increased significantly at 1 and 3 dpi. However, they decreased to very low levels from 7 to 28 dpi. On the contrary, the M2-type MG decreased significantly after SCI and remained at a low level during the pathological process.

The polarization of microglia and infiltrated macrophages in the injured mice spinal cords: A dynamic analysis

Jing-Lu Li[1, 2&], Gui-Qiang Fu[1, 2&], Yang-Yang Wang[1, 2&], Ming-Ming Bian[1, 2], Yao-Mei Xu[1, 2], Lin Zhang[1, 2], Yu-Qing Chen[1, 2], Nan Zhang[1, 2], Shu-Qin Ding[1, 2], Rui Wang[2], Rui Fang[3], Jie Tang[2], Jian-Guo Hu[1, 2*], He-Zuo Lü[1, 2*]

[1] Clinical Laboratory, the First Affiliated Hospital of Bengbu Medical College, Bengbu, Anhui 233004, P.R. China

[2] Anhui Key Laboratory of Tissue Transplantation, the First Affiliated Hospital of Bengbu Medical College, Bengbu, Anhui 233004, P.R. China

[3] Department of Clinical Medical, Bengbu Medical College, Bengbu, Anhui 233030, P.R. China

& These authors contributed equally to this work

* Co-corresponding authors:

Jian-Guo Hu

Email address: jghu9200@163.com

He-Zuo Lü

Email address: lhz233003@163.com

Please address correspondence to:

He-Zuo Lü, M.D. Ph.D., Professor

Anhui Key Laboratory of Tissue Transplantation

the First Affiliated Hospital of Bengbu Medical College

287 Chang Huai Road

Bengbu 233004, P.R. China

Tel: +86-552-3170692

E-mail: lhz233003@163.com

Abstract

Background. Following spinal cord injury (SCI), a large number of peripheral monocytes infiltrate into the injured area and differentiate into macrophages (Mø). These monocyte-derived Mø are very difficult to distinguish from the local activated microglia (MG). Therefore, the term Mø/MG are often used to define the infiltrated Mø and/or activated MG. It has been recognized that pro-inflammatory M1-type Mø/MG play "bad guy" roles in the pathological mechanism of SCI. Our recent research showed that in sub-acute spinal cord injured mice local M1 cells are mainly $CD11b^{+}CD45^{-/low}CD68^{+}$. Therefore, we speculated that the M1 cells in the injured spinal cords mainly derived from MG rather than infiltrating Mø. And so far, their dynamics after SCI are not completely clear.

Methods. Using an Infinite Horizon impactor, the female BALB/c mouse SCI model was made by using a 1.3 mm diameter rod and a 50 Kdynes force. Sham-operated (sham) mice only received a laminectomy without contusive injury. Fow cytometry and immunohistofluorescence were combined to analyze the dynamic changes of polarized Mø and MG in the acute (1 day), subacute (3, 7 and 14 days) and chronic (21 and 28 days) phases of SCI.

Results. The total Mø/MG gradually increased and peaked at 7 days post-injury (dpi), and maintained at high levels 14, 21 and 28 dpi. Most of the Mø/MG were activated, and the Mø increased significantly at 1 and 3 dpi. However, with the pathological process, the activated MG increased nearly to 90% at 7, 14, 21 and 28 dpi. Both M1 and M2 Mø were increased significantly at 1 and 3 dpi. However, they decreased to very low levels from 7 to 28 dpi. On the contrary, the M2-type MG decreased significantly after SCI and remained at a low level during the pathological process.

Introduction

Spinal cord injury (SCI) is a is a serious disabling neurological disease, which caused by traffic accidents, trauma and other reasons (Attal 2021; Perrouin-Verbe et al. 2021; Quadri et al. 2020). As the bridge between the brain and peripheral nerves, the nerves from spinal cord are distributed to the skin, muscles and various internal organs, once it is damaged, it will cause serious pathophysiological changes. For patients, SCI brings serious physical and mental pain. For families and society, it also causes serious economic and social burdens. (Chay & Kirshblum 2020). Therefore, to find effective treatment strategies, we must deeply explore its pathological mechanism.

After SCI, the local microenvironment is destroyed (Anjum et al. 2020; Fan et al. 2022; Fan et al. 2018). At the tissue level, SCI leads to blood-brain barrier destruction, local tissue ischemia and hypoxia, demyelination, and glial scar formation (Anjum et al. 2020). Following SCI, the secretion of neurotrophins and anti-inflammatory factors decreased, while the production of oxygen free radicals, excitatory amino acids and pro-inflammatory factors increased (Hao et al. 2017; Harrington et al. 2004). In addition, at the cellular level, SCI not only leads to neuronal and oligodendrocyte necrosis and astrocyte activation, it also includes the response of immune cells, such as the local MG activation and the peripheral immune cell infiltration (Donnelly & Popovich 2008; Lee et al. 2009). Among the immune cells, some have neuroprotective functions, while others are destructive. The final results of SCI depend on the dynamic balance of these cells (DiSabato et al. 2016; Wolf et al. 2002). However, which immune cell population play key role? So far, it is still an open question.

Previous studies found that local pro-inflammatory M1-type MG (MG) and/or infiltrated M1-type Mø are absolutely dominant following SCI (Fan et al. 2019; Sato et al. 2012). These suggest that M1 cells may be the key factor for the imbalance of local immune microenvironment of SCI. However, so far, it is still a controversial topic that the increasing of M1 cells mainly come from MG or the infiltrated Mø. For example, it was previously reported that MG play a central role in modulating of neuroinflammatory response following SCI (Brockie et al. 2021). The other also reported that inhibiting MG proliferation could improve recovery in mice and non-human primates after SCI (Poulen et al. 2021). However, many scholars believe that both MG and infiltrated Mø play the important roles in the microenvironment of SCI, and it likes a "double-edged sword", which play both neuroprotective and neurodamaging effects (Devanney et al. 2020; Ding et al. 2021). Our recent research showed that in subacute spinal cord injured mice local M1 cells are mainly $CD11b^{+}CD45^{-/low}CD68^{+}$, rather than $CD11b^{+}CD45^{high}CD68^{+}$ cells (Chen et al. 2021; Chen et al. 2020). Therefore, we speculated that the M1 cells in the injured spinal cords mainly derived from MG rather than infiltrating Mø. In addition, the dynamics of these cells after SCI are not completely clear. Because at the early stage of SCI, mice cannot urinate autonomously and need artificial assistance. Due to the anatomical differences of urinary system, using the female could reduce the pain, infection and mortality of animals. In this study, we used only female mice. Therefore, in this study, the female BALB/c mouse SCI model was made, the activation and proportion of MG and infiltrated Mø at different time points after SCI were dynamically observed by a panel of specific cell markers using flow cytometry (FCM) and immunohistofluorescence (IHF).

Materials & Methods

Animals

A total of 150 specific-pathogen free adult female C57BL/6 mice (18–20 g) were obtained from Chang Zhou Cavens Laboratory Animal Ltd. (Chang Zhou, China; license No. SCXK (Su) 2016-0010). The mice were kept in a suitable environment with relative humidity of 40%-60% and temperature of 21-25 °C, 60 air exchanges per hour in the cages, and a 12/12-hour light/dark cycle with the lights on at 7:00 AM. All experimental designs and reports were referred to previous to the previous guidelines (Kilkenny et al. 2011). The surgery protocol was approved by the Animal Care Ethics Committee of Bengbu Medical College. The number of Animal Ethical Approval was 2017-037. The mice were randomly divided into sham-operated (sham), 1-, 3-, 7-, 14-, 21- and 28-days post-injury (dpi) groups, using a computer based random order generator (Zhao et al. 2018). The comprehensive description of the total number of mice used is shown in Figure 1.

Contusive SCI

The mice contusive SCI model was established by using an Infinite Horizon impactor (Precision Systems & Instrumentation, Lexington, KY, USA), as our previously method (Chen et al. 2021; Chen et al. 2020). Inclusion criteria: the animals were undergoing successful contusive SCI, defined by the T9 site was filled with blood and edema, and the spinal cord was intact and not ruptured. Exclusion criteria: the degree of injury is not up to the standard, postoperative infection or sacrifice. Briefly, the mice were anesthetized with 80 mg/kg ketamine and 10 mg/kg xylazine (both obtained by Sigma-Aldrich, St. Louis, MO, USA), then the vertebral lamina of T9 was removed, and the spines of T7 and T11 were stabilized with forceps. The T9 spinal cord was impacted with 50Kdynes force, and the diameter of the impact rod was 1.3 mm. After the impact, the spinal cord was filled with blood and edema. For the sham group, the T9 vertebral lamina

only be resected without impact. After operation, the mice were kept in a suitable environment with relative humidity of 40%-60% and temperature of 21-25 °C. Bladder emptying was carried out three times a day, and the health status were observed and recorded. At the same time, meloxicam (5mg/kg, CSN pharm, IL, USA) and chloramphenicol (50mg/kg, Sangon Biotech, Shanghai, China) were injected subcutaneously daily 7 days after surgery to alleviate pain and prevent infection. Due to it is necessary to collect spinal cord specimens injured at different time points, the experimenter could not be blinded to whether the animal belongs to which group.

Flow cytometry

At the corresponding time points after surgery, mice were euthanized as mentioned above. After the mice were completely euthanized, the chest cavity was opened with surgical scissors to expose the heart. The ventricle was clamped with a vascular clamp to fix the heart. The No.7 needle was inserted into the left ventricle. At the same time, a small opening was cut on the right atrium so that the blood and lavage solution can be drained. Then, 10ml of 0.01M phosphate-buffered saline (PBS) buffer solution (pH = 7.4) was slowly injected at 250 ml/h with a microinjection pump. After perfusion, the 5 mm spinal cord segments which contained the injury center were taken, and the corresponding spinal cord segments were also obtained from the sham group. The spinal cords of different groups were put into the 45-μm nylon mesh and fully ground with the syringe plunger to obtain single cell suspensions. To obtain enough cells for analysis, 3 spinal cord segments were mixed for one test. The Percoll gradient centrifugation (Amersham Pharmacia Biotech, Piscataway, NJ, USA) was used to separate the single cells. (Chen et al. 2021; Chen et al. 2020). Table 1 showed the fluorescent labeled antibodies which used in this study to identify different immune cell subtypes. The immunoglobulin with the same species, subtype, dose and fluorescein as the primary antibody was used as the isotype control to eliminate the background staining caused by the non-specific binding of the antibody. The cells were collected using a BD Accuri flow cytometer (Becton Dickinson, San Diego, CA, USA), and data were analyzed using FlowJo7.6.1 software (FlowJo, LLC, Ashland, OR, USA).

Immunofluorescence double-staining

At the indicated time points post-injury, mice were euthanized as mentioned above. Then, the mice were perfused with 10mL 0.01 M PBS at 250 mL/h with a microinjection pump with an injection pump, followed by 10 mL of 4% paraformaldehyde (PFA) at a rate of 180 mL/h. After perfusion, the 5 mm spinal cord segments which contained the injury center were taken, and the corresponding spinal cord segments were also obtained from the sham group. The spinal cords were then fixed in 10 mL of 4% PFA solution at 4°C overnight. The next day, the spinal cords were removed from the 4% PFA solution and placed in the 20% sucrose solution (prepared in PBS) at 4°C overnight. To the third day, the spinal cords transferred to the 30% sucrose at 4°C, until the samples sinking to the bottom of the solution. This process usually needs one day. Next, the embedding agent (Tissue-Tek, Sakura Finetek USA Inc., Torrance, CA, USA) was used to embed the spinal cord segments at -20°C. The 6 μm thick transverse sections were cut by using a Leica CM1900 cryostat (Leica Microsystems, Bannockburn, IL, USA). The IHF assay was performed as previously described (Chen et al. 2021; Chen et al. 2020). Briefly, the slides were washed three times with 0.01 M PBS to completely clear the embedding agent. When the slides were left to dry, the blocking solution (0.01 M PBS containing 10% normal goat serum) were used for 2 hours at room temperature to eliminate the background staining caused by the non-specific binding of the antibody. After cleaning the blocking solution, the primary antibodies with appropriate concentration were incubated overnight at 4°C. The next day, the slides were washed three times with 0.01 M PBS to completely remove the unbound antibodies. Then, the

secondary antibodies with appropriate concentration were incubated at 37°C for 1 hour. The primary and FITC and RHO-conjugated secondary antibodies were shown in Table 1. After the second antibody incubation, the 0.01 M PBS was used to wash the slides for three times, and the 1 μg/ml Hoechst 33342 (Sigma-Aldrich; Cat# B2261) containing medium was used to coverslip the slides. Finally, the slides were examined using a ZWISS Axio observation microscope (Carl Zeiss, Oberkochen, Germany). The cell quantification was performed as previously described (Chen et al. 2021; Chen et al. 2020). Briefly, for each spinal cord, the cells of 5 complete cross-sections containing the injury epicenter (0 mm), rostral (1 mm and 0.5 mm) and caudal (-1 mm and -0.5 mm) were counted.

Statistical analyses

The SPSS software v.14.0 (SPSS Inc., Chicago, IL, USA) was used to statistical analysis. The non-parametric Kruskal Wallis analysis of variance (ANOVA) following by the individual Mann-Whitney U test was used. The $P < 0.05$ was considered to be statistically significant.

Results

Temporal pattern of MG and infiltrated Mø following SCI: the flow cytometry (FCM) analysis

To determine the temporal pattern of MG and infiltrated Mø in the spinal cords of sham, 1, 3, 7, 14, 21 and 28 dpi, a panel of cell markers (CD11b, CD45 and CD68) was examined by FCM. Considering that CD45 is not only a common marker of peripheral leukocytes, it can also be expressed at a low level in MG (Sedgwick et al. 1998), CD11b is mainly expressed in MG and monocyte-derived Mø (Martin et al. 2017), and CD68 is the common marker of activated MG and Mø (Chen et al. 2015; Greaves & Gordon 2002), $CD45^{high}$ population was defined as peripheral infiltrated leukocytes, $CD68^{+}CD11b^{+}$ population was activated Mø and MG, $CD45^{high}CD11b^{+}$ population was peripheral infiltrated Mø, $CD45^{-/low}CD11b^{+}$ population was MG, $CD45^{high}CD68^{+}CD11b^{+}$ population was activated peripheral infiltrated Mø, $CD45^{-/low}CD68^{+}CD11b^{+}$ population was activated MG, and $CD45^{high}CD68^{-}CD11b^{-}$ population was peripheral infiltrated leukocytes excluding Mø (Figure 2A).

Figure 2B showed that the percentages of $CD11b^{+}$ cells in the groups of sham, 1, 3, 7, 14, 21 and 28 dpi were 6.59%, 6.53%, 6.31%, 18.18%, 12.69%, 12.11% and 12.56%, respectively. The percentages of $CD11b^{+}$ cells among sham, 1 and 3 dpi groups had no significant difference ($P > 0.05$, $n = 6$). However, at 7 dpi, the proportion increased significantly and reached to peak, although the proportions decreased at the later time points (14, 21 and 28 dpi), they still continued at high levels comparing with sham,1 and 3 dpi groups ($P < 0.01$, $n = 6$).

Figure 2C showed that the percentages of $CD68^{+}$ cells in the groups of sham, 1, 3, 7, 14, 21 and 28 dpi were 9.87%, 19.91%, 20.43%, 39.47%, 37.40%, 30.75% and 31.87%, respectively. The percentage of $CD68^{+}$ cells in the sham-operated spinal cords was the lowest comparing with the injured groups, and there were statistically significant differences ($P < 0.01$, $n = 6$). The proportions increased significantly after injury, and reached to peak at 7 dpi, and continued at high levels at 14, 21 and 28 dpi. There were no significant differences among 7, 14, 21 and 28 dpi ($P > 0.05$, $n = 6$). However, the percentages of $CD68^{+}$ cells in these four groups were significant higher comparing with sham ($P < 0.01$, $n = 6$), 1 and 3 dpi ($P < 0.05$, $n = 6$).

Figure 2D showed that the percentages of $CD11b^{+}CD68^{+}$ cells in the groups of sham, 1, 3, 7, 14, 21 and 28 dpi were 1.33%, 4.95%, 4.54%, 15.50%, 10.19%, 8.48% and 9.47%, respectively. In the sham-operated spinal cords, $CD11b^{+}CD68^{+}$ cells were extremely rare, however, they increased significantly in the injured groups (comparing with sham, $P < 0.01$, $n = 6$). The

proportions had no significant differences between 1 and 3 dpi ($P > 0.05$, $n = 6$). However, it reached to peak at 7 dpi. Subsequently, the percentages of cells decreased, but remained at high levels at 14, 21 and 28 dpi. There were no significant differences among 14, 21 and 28 dpi ($P > 0.05$, $n = 6$). Although, the percentages of $CD11b^{+}CD68^{+}$ cells in these three groups were lower than that of 7 dpi group ($P < 0.05$, $n = 6$), they were still significant higher comparing with sham, 1 and 3 dpi ($P < 0.01$, $n = 6$).

Figure 2E showed that the percentages of $CD45^{high}$ cells in the groups of sham, 1, 3, 7, 14, 21 and 28 dpi were 2.65%, 5.63%, 7.16%, 12.51%, 15.67%, 8.76% and 9.64%, respectively. In the sham-operated spinal cords, $CD45^{+}$ cells were extremely rare, and these cells gradually increased after injury, peaked at 7 and 14 dpi, and then decreased, but still maintained at high levels at 21 and 28 dpi. There was no significant statistical difference between 7 and 14 dpi ($P > 0.05$, $n = 6$). However, comparing with the other groups, the percentages of $CD45^{high}$ cells in these two groups had significant differences ($P < 0.05$ or 0.01, $n = 6$).

Figure 2F showed that the percentages of $CD11b^{+}CD45^{high}$ cells in the groups of sham, 1, 3, 7, 14, 21 and 28 dpi were 1.35%, 3.85%, 4.26%, 5.41%, 4.13%, 2.57% and 3.04%, respectively. In the sham-operated spinal cords, $CD11b^{+}CD45^{high}$ cells were also extremely rare, and these cells significantly increased after injury, peaked at 7 dpi, and then decreased, but still maintained at high levels at 14, 21 and 28 dpi. Comparing with the other groups, the percentage of $CD11b^{+}CD45^{high}$ cells in 7 dpi group had significant differences ($P < 0.05$ or 0.01, $n = 6$). In addition, it should be emphasized that the proportion of $CD11b^{+}CD45^{high}$ cells in each group is significantly lower than that of their corresponding $CD11b^{+}$ cells (Figure 2B). This indicates that the proportion of peripheral infiltrated Mø is significantly lower than that of MG in the injured spinal cords.

Figure 2G showed that the percentages of $CD11b^{+}CD45^{-/low}$ cells in the groups of sham, 1, 3, 7, 14, 21 and 28 dpi were 3.90%, 2.73%, 2.70%, 13.89%, 8.72%, 10.16% and 8.41%, respectively. Among sham, 1 and 3 dpi groups, the percentages of $CD11b^{+}CD45^{-/low}$ cells had no significant difference ($P > 0.05$, $n = 6$). However, at 7 dpi, the proportion increased significantly and reached a peak, although the proportions decreased at the later time points (14, 21 and 28 dpi), they still continued at high levels comparing with sham,1 and 3 dpi groups ($P < 0.01$, $n = 6$). Comparing with the other groups, the percentage of $CD11b^{+}CD45^{-/low}$ cells in the 7 dpi was significantly higher ($P < 0.05$ or 0.01, $n = 6$). In addition, it should be emphasized that except for the 1 and 3 dpi groups, $CD11b^{+}CD45^{-/low}$ cells constitute the majority of $CD11b^{+}$ cells (Figure 2B). This shows that except for the two early time points of 1 and 3 dpi, MG are dominant in proportion to peripheral infiltrated Mø in the injured spinal cord.

Figure 2H showed that the percentages of $CD68^{+}CD45^{high}$ cells in the groups of sham, 1, 3, 7, 14, 21 and 28 dpi were 0.53%, 3.54%, 4.53%, 3.74%, 4.06%, 4.10% and 4.08%, respectively. In the sham-operated spinal cords, $CD68^{+}CD45^{high}$ cells were also extremely rare, and these cells rapidly increased after injury. Up to 28 dpi, they still maintained at high levels. Comparing with the sham group, the percentages of $CD68^{+}CD45^{high}$ cells in the injured groups were significantly higher ($P < 0.01$, $n = 6$). There were no significant differences among the injured groups ($P > 0.05$, $n = 6$). In addition, it should be emphasized that the proportion of $CD68^{+}CD45^{high}$ cells in each SCI group is significantly lower than that of their corresponding $CD68^{+}$ cells (Figure 2C). This preliminarily indicates that the proportion of activated peripheral infiltrated Mø is significantly lower than that of activated MG in the injured spinal cords.

Figure 2I showed that the percentages of $CD68^{+}CD45^{-/low}$ cells in the groups of sham, 1, 3, 7, 14, 21 and 28 dpi were 9.17%, 19.18%, 16.59%, 34.83%, 36.30%, 25.57% and 25.32%,

respectively. The percentage of $CD68^{+}CD45^{-/low}$ cells in the sham-operated spinal cords was the lowest comparing with the injured groups ($P < 0.05$ or 0.01, $n = 6$). The proportions had no significant differences at 1 and 3 dpi ($P > 0.05$, $n = 6$). However, they reached to peak at 7 and 14 dpi, and remained at high levels at 21 and 28 dpi. Among 7, 14, 21 and 28 dpi, there were no significant differences ($P > 0.05$, $n = 6$). In addition, it should be emphasized that the proportion of $CD68^{+}CD45^{-/low}$ cells in each SCI group is significantly lower than that of their corresponding $CD68^{+}$ cells (Figure 2C). This preliminarily indicates that the activated MG is dominant in proportion to activated peripheral infiltrated Mø in the injured spinal cord.

Figure 2K showed that the percentages of $CD68^{+}CD11b^{+}CD45^{high}$ cells in the groups of sham, 1, 3, 7, 14, 21 and 28 dpi were 0.25%, 2.45%, 2.73%, 1.61%, 1.15%, 1.39% and 1.23%, respectively. In the sham-operated spinal cords, $CD68^{+}CD11b^{+}CD45^{high}$ cells were extremely rare, and these cells rapidly increased after injury, peaked at 1, 3 and 7 dpi. Comparing with sham-operated spinal cords, these cells in the 1, 3 and 7 dpi groups are significantly more ($P < 0.01$, $n = 6$). Although, comparing with 1, 3 and 7 dpi groups, the proportions decreased to the lower levels at the later time points (14, 21 and 28 dpi) ($P < 0.05$, $n = 6$), they still maintained at higher levels comparing to the sham-operated group ($P < 0.05$, $n = 6$). In addition, it should be emphasized that the combined application of the three markers is more precise for defining activated peripheral infiltrated Mø. Comparing with Figure 2H, the proportion of cells in Figure 2K is lower. This accurately indicates that the activated peripheral infiltrated Mø in the injured spinal cord are significantly inferior to activated MG.

Figure 2L showed that the percentages of $CD68^{+}CD11b^{+}CD^{45-/low}$ cells in the groups of sham, 1, 3, 7, 14, 21 and 28 dpi were 3.61%, 7.54%, 13.10%, 18.15%, 11.06%, 7.03% and 7.48%, respectively. In the sham-operated spinal cords, $CD68^{+}CD11b^{+}CD^{45-/low}$ cells were also extremely rare, and these cells gradually increased after injury, peaked at 7 dpi (comparing with the other groups, $P < 0.01$, $n = 6$), and then decreased, but still maintained at high levels at 14, 21 and 28 dpi. Comparing to the sham-operated group, the percentages of $CD68^{+}CD11b^{+}CD^{45-/low}$ cells in all SCI groups had significant differences ($P < 0.01$, $n = 6$). It should be emphasized that this part of the results is the essence of this study. It not only shows the dynamics of MG activation after SCI, but also clearly confirms that the activated MG are absolutely dominant in the injured spinal cord.

Temporal pattern of MG and infiltrated Mø following SCI: the immunohistofluorescence (IHF) analysis

To verify the temporal pattern of MG and infiltrated Mø detected by FCM, several representative spinal cords (sham, 1, 7 and 28 dpi) were selected for IHF analysis. CD11b, CD68 and TMEM119 antibodies were used for immunofluorescence labeling (Figure 3). Here, CD11b is the common marker of MG and monocyte-derived Mø (Martin et al. 2017), CD68 is the common marker of activated MG and Mø (Chen et al. 2015; Greaves & Gordon 2002), and TMEM119 is the specific marker of MG (Bohnert et al. 2020).Therefore, $TMEM119^{+}CD11b^{+}$ cells are total MG, $TMEM119^{-}CD11b^{+}$ cells are monocyte-derived Mø, $TMEM119^{+}CD68^{+}$ cells are activated MG, $TMEM119^{-}CD68^{+}$ cells are activated monocyte-derived Mø, respectively (Figure 3A-H). The representative images showed that $TMEM119^{+}CD11b^{+}$ cells could be detected in all groups (Figure 3A-D). The statistical results (Figure 3E) showed that the number (cells/mm^2) of $TMEM119^{+}CD11b^{+}$ cells had no significant difference between sham (117.50 ± 19.30) and 1 dpi (200.33 ± 16.59) groups ($P > 0.05$, $n = 6$). Comparing with the other three groups, there were most $TMEM119^{+}CD11b^{+}$ cells in 7 dpi (537.33 ± 99.80) ($P < 0.01$, $n = 6$). Although, the cells were decreased at 28 dpi (308.33 ± 50.27), the number still significantly more comparing with

sham and 1 dpi groups ($P < 0.01$, $n = 6$). In the sham-operated spinal cords, TMEM119^{-}CD11b^{+} cells were extremely rare (Figure 3A), and they significantly increased in the three SCI groups (Figure 3B-D). The statistical results (Figure 3F) showed that the numbers of TMEM119^{-} CD11b^{+} cells in all three SCI groups were significant more than that of sham (70.17 ± 7.65) group ($P < 0.01$, $n = 6$). Comparing with the other three groups, there were also most TMEM119^{-} CD11b^{+} cells in 7 dpi (201.80 ± 42.53) group ($P < 0.05$, $n = 6$). There was no significant statistical difference between 1 (144.83 ± 9.45) and 28 dpi (155.20 ± 62.30) groups ($P > 0.05$, $n = 6$).

In the representative images of Figure 4A, both TMEM119^{+}CD68^{+} and TMEM119^{-}CD68^{+} cells were extremely rare in sham-operated spinal cords. However, both of them could be detected in all SCI groups (Figure 4B-D). The statistical results (Figure 4E and F) showed that the numbers of these two types of cells had significant differences among sham and SCI groups ($P < 0.01$, $n = 6$). Comparing with the three other groups, there were most TMEM119^{+}CD68^{+} cells in 7 dpi (473.50 ± 64.48) group ($P < 0.01$, $n = 6$). Although, the number of these cells decreased at 28 dpi (269.67 ± 42.49), it still significantly more comparing with sham (6.67 ± 6.31) and 1 dpi (156 ± 43.75) groups ($P < 0.01$, $n = 6$). Comparing with the other two groups, TMEM119^{-}CD68^{+} cells were most in 1 (155.00 ± 18.51) and 7 dpi (124.75 ± 34.88) groups ($P < 0.01$, $n = 6$). Although, the cells decreased at 28 dpi (61.33 ± 25.24), their number still significantly more comparing with sham (0.00 ± 0.00) group ($P < 0.01$, $n = 6$).

The above analysis showed that the verification results of IHF are basically consistent with the temporal pattern of MG and infiltrated Mø in the injured spinal cords detected by FCM.

Temporal pattern of SCI-induced M1 and M2 differentiation of Mø and MG: the FCM analysis

To further explore the temporal pattern of SCI-induced M1 and M2 differentiation of Mø and MG, FCM was used by combining CD68, CD45, CD11b and CCR7 antibodies. Here, CD11b^{+}CD68^{+}CCR7^{+} subpopulation was defined as total M1 cells, CD11b^{+}CD68^{+}CCR7^{-} subpopulation was defined total M2 cells, CD11b^{+}CD45$^{-/low}$CD68^{+}CCR7^{+} subpopulation was defined as MG-derived M1 cells, CD11b^{+}CD45$^{-/low}$CD68^{+}CCR7^{-} cells subpopulation was defined MG-derived M2 cells, CD11b^{+}CD45^{high}CD68^{+}CCR7^{+} subpopulation was defined as peripheral infiltrated M1 cells, CD11b^{+}CD45^{high}CD68^{+}CCR7^{-} subpopulation was defined as peripheral infiltrated M2 cells(Chen et al. 2021; Chen et al. 2020).

As shown in Figure 5A, the same size “region” of total CD11b^{+} cells (R1) were set for each sample in the pseudocolor plots of CD45/CD11b, and then the percentage of each cell population was analyzed in the pseudocolor plots of CD68/CCR7 by setting the boundary between negative and positive with isotype-matched antibodies. The statistical results (Figure 5B) showed that the percentage of CD11b^{+}CD68^{+}CCR7^{+} cells in the sham-operated spinal cords was the lowest (10.45%) comparing with the injured groups, and there were statistically significant ($P < 0.01$, $n = 6$). The proportions significantly increased after injury (1 dpi, 36.25% and 3 dpi, 52.02%), and reached to peak from 7 dpi (58.17%), and maintained at high levels at 14 (63.83%), 21 (68.35%) and 28 dpi (60.28%). There were no significant differences among 7, 14, 21 and 28 dpi ($P > 0.05$, $n = 6$). However, the percentages of CD11b^{+}CD68^{+}CCR7^{+} cells in these four groups were significant higher comparing with sham and 1 dpi ($P < 0.01$, $n = 6$).

Figure 5C showed that the percentages of CD11b^{+}CD68^{+}CCR7^{-} cells in the groups of sham, 1, 3, 7, 14, 21 and 28 dpi were 15.42%, 8.73%, 17.76%, 19.92%, 9.53%, 15.77% and 15.92%, respectively. Among all groups, there were no significant differences ($P > 0.05$, $n = 6$). However, when converted to total M1/M2 ratio, its temporal pattern was obvious. As shown in Figure 5D,

the total M1/M2 ratios in sham, 1, 3, 7, 14, 21 and 28 dpi were 0.69 ± 0.31, 4.76 ± 1.97, 3.92 ± 1.19, 3.97 ± 0.43, 5.71 ± 2.01, 4.77 ±1.55 and 3.85 ± 0.52, respectively. The ratio was very low in the sham-operated spinal cords and significantly increased after SCI. Comparing with the sham group, the ratios in all SCI groups were significant increased ($P < 0.01$, $n = 6$). However, among all SCI groups, the ratios had no significant differences ($P > 0.05$, $n = 6$).

As shown in Figure 5E, in the pseudocolor plots of CD11b/CD45, the same size "region" of $CD11b^{+}CD45^{-/low}$ cells (R2) were set for each sample, and then the percentages of cell populations were analyzed same as Figure 5A. The statistical results (Figure 5F) showed that the percentage of $CD11b^{+}CD45^{-/low}CD68^{+}CCR7^{+}$ cells in the sham-operated spinal cords was the lowest (11.45%) comparing with the injured groups, and the differences were statistically significant ($P < 0.01$, $n = 6$). The proportions significantly increased after injury (1 dpi, 44.90%; 3 dpi, 59.70% and 7 dpi, 61.65%), and reached to peak at 14 (73.72%) and 21 dpi (70.48%), and continued at high level at 28 dpi (63.17%). There were no significant differences among the groups of 3, 7 and 28 dpi, and between 7 and 21 dpi ($P > 0.05$, $n = 6$). However, the percentages in the groups of 3, 7, 14, 21 and 28 dpi were significantly higher than that of 1 dpi ($P < 0.05$ or 0.01, $n = 6$).

Figure 5G showed that the percentages of $CD11b^{+}CD45^{-/low}CD68^{+}CCR7^{-}$ cells in the groups of sham, 1, 3, 7, 14, 21 and 28 dpi were 20.35%, 8.52%, 19.38%, 18.47%, 10.37%, 17.30% and 18.05%, respectively. Among all groups, there were no significant differences ($P > 0.05$, $n = 6$). However, when converted to total M1/M2 ratio, its temporal pattern was more obvious. As shown in Figure 5H, the M1/M2 ratios of MG in the groups of sham, 1, 3, 7, 14, 21 and 28 dpi were 0.62 ± 0.36, 4.48 ± 1.02, 3.29 ± 0.91, 3.52 ± 0.92, 7.03 ± 2.05, 4.26 ± 1.10 and 3.53 ± 0.62, respectively. The ratio was very low in sham group and increased after SCI, peaked at 7 dpi, and then decreased at 21 and 28 dpi. In the group of 7 dpi, the ratio of was significantly higher than those of the other groups ($P < 0.05$, $n = 6$). Among the groups of 1, 3, 21 and 28 dpi, the ratios had no significant differences ($P > 0.05$, $n = 6$). However, they still maintained at high levels comparing with the sham-operated spinal cords ($P < 0.01$, $n = 6$).

In Figure 5I, in the pseudocolor plots of CD11b/CD45, the same size "region" of $CD45^{high}CD11b^{+}$ cells (R3) were set for each sample, and then the percentages of cell populations were analyzed same as Figure 5A. Figure 5J showed that the percentages of $CD11b^{+}CD45^{high}CD68^{+}CCR7^{+}$ cells in the groups of sham, 1, 3, 7, 14, 21 and 28 dpi were 4.70%, 29.29%, 45.38%, 48.80%, 57.20%, 59.16% and 70.35%, respectively. The cell percent showed an increasing trend after SCI, and reached the highest levels at 28 dpi. However, there were no significant differences among the groups of 7, 14, 21 and 28 dpi ($P > 0.05$, $n = 6$), which were statistically significant comparing with the groups of sham and 1dpi ($P < 0.05$ or 0.01, $n = 6$). In Figure 5K, the percentages of $CD11b^{+}CD45^{high}CD68^{+}CCR7^{-}$ cells in the groups of sham, 1, 3, 7, 14, 21 and 28 dpi were 3.69%, 4.37%, 20.30%, 18.10%, 7.80%, 4.37% and 3.46%, respectively. The cell percentages were highest at 3 and 7 dpi, which were statistically significant comparing with the other groups ($P < 0.01$, $n = 6$). However, among the groups of sham, 1, 14, 21 and 28 dpi, the differences were not significant ($P > 0.05$, $n = 6$).

When converted to the ratio of infiltrated M1/M2, its temporal pattern was more obvious. As shown in Figure 5l, the infiltrated M1/M2 ratios in the groups of sham, 1, 3, 7, 14, 21 and 28 dpi were 1.26 ± 0.36, 7.92 ± 4.67, 2.30 ± 0.47, 3.30 ± 1.06, 7.78 ± 1.99, 14.84 ± 5.47 and 22.16 ± 7.11, respectively. The ratio was very low in sham group, and there was a transient rise at 1 dpi. Then, it decreased to sham level at 3 and 7 dpi, and then the ratio showed an increasing trend from 14 to 28 dpi, it reached the highest levels at 28 dpi. Among sham, 3 and 7 dpi groups, the

ratios had no significant differences ($P > 0.05$, $n = 6$). However, comparing with the other groups, the ratios were significant lower ($P < 0.05$ or 0.01, $n = 6$).

Temporal pattern of SCI-induced M1 and M2 differentiation of Mø and MG: the IHF analysis

To verify the temporal pattern of SCI-induced M1 and M2 differentiation of Mø and MG detected by FCM, several representative spinal cords (sham, 1, 7 and 28 dpi) were selected for IHF analysis. CD68, TMEM119, CCR7 and Arg1 antibodies were used for immunofluorescence labeling (Figures 6 and 7). Here, $CD68^+CCR7^+$ and $CD68^+Arg1^+$ label total M1 and M2 cells, respectively (Figure 6); $TMEM119^+$ $CCR7^+$ and $TMEM119^+Arg1^+$ cells are M1 and M2 MG, respectively (Figure 7A-J). Therefore, ($CD68^+CCR7^+$ minus $TMEM119^+CCR7^+$) and ($CD68^+Arg1^+$ minus $TMEM119^+Arg1^+$) are M1 and M2 monocyte-derived Mø, respectively (Figure 7K and L).

The representative images showed that $CD68^+CCR7^+$, $CD68^+Arg1^+$, $TMEM119^+CCR7^+$ and $TMEM119^+Arg1^+$ cells were both extremely rare in sham-operated spinal cords (Figures 6A and E, 7A and E). However, these cells could be detected in all SCI groups (Figure 6B-D, F-H, and 7B-D, F-H).

The statistical results (Figure 6I) showed that the numbers of $CD68^+CCR7^+$ cells in the groups of sham, 1, 7 and 28 dpi were 2.67 ± 2.50, 235.33 ± 5.13, 577.17 ± 40.18 and 543.17 ± 31.35, respectively. All SCI groups were significant more than that of sham-operated spinal cords ($P < 0.01$, $n = 6$). Up to 7 dpi, the cell number reached to peak, and continued at high levels at 28 dpi. The differences were not significant between 7 and 28 dpi ($P > 0.05$, $n = 6$). However, both of them were more than 1 dpi ($P < 0.01$, $n = 6$).

In Figure 6J, the numbers of $CD68^+Arg1^+$ cells in the groups of sham, 1, 7 and 28 dpi were 3.83 ± 3.43, 105.33 ± 9.56, 72.83 ± 10.55 and 150.17 ± 22.21, respectively. Although, all SCI groups were significant more than sham group in the numbers of $CD68^+Arg1^+$ cells ($P < 0.01$, $n = 6$), the 7 dpi had the least number of cells among the three SCI groups, and there were most cells in 28 dpi group. The pairwise comparisons of the three SCI groups were statistically significant ($P < 0.01$, $n = 6$).

In Figure 7I, the numbers of $TMEM119^+CCR7^+$ cells in the groups of sham, 1, 7 and 28 dpi were 3.17 ± 1.83, 205.17 ± 9.97, 412.33 ± 18.04 and 410.17 ± 50.92, respectively. The overall change trend of cell number was similar to that of $CD68^+CCR7^+$ cells. Figure 7J showed that the numbers of $TMEM119^+Arg1^+$ cells in the groups of sham, 1, 7 and 28 dpi were 4.33 ± 2.42, 85.83 ± 10.68, 50.00 ± 4.29 and 125.00 ± 13.33, respectively. The overall trend was also similar to that of $CD68^+Arg1^+$ cells.

In Figure 7K, the numbers of infiltrated $CD68^+CCR7^+$ cells in the groups of sham, 1, 7 and 28 dpi were 0.00 ± 0.00, 30.17 ± 11.72, 164.83 ± 45.64 and 133.00 ± 56.67, respectively. All SCI groups were significant more than that of sham-operated spinal cords ($P < 0.01$, $n = 6$). Up to 7 dpi, the cell number reached to peak. Although the number of cells had a decreasing trend, it remained at a higher level at 28 dpi. The difference was not significant between 7 and 28 dpi ($P > 0.05$, $n = 6$). However, both of them were more than 1 dpi ($P < 0.01$, $n = 6$). Figure 7L showed that although the numbers of infiltrated $CD68^+Arg1^+$ cells could be detected in SCI groups, they were very rare in all groups. The numbers in the groups of sham, 1, 7 and 28 dpi were 0.00 ± 0.00, 19.50 ± 12.65, 22.83 ± 12.04 and 25.17 ± 15.74, respectively. All three SCI groups were significant more than that of sham group ($P < 0.01$, $n = 6$). Among the SCI groups, there were no significant differences ($P > 0.05$, $n = 6$).

The above analysis showed that the results of IHF are basically consistent with the M1 and M2 differentiation of Mø and MG detected by FCM.

Summary of dynamic changes of MG, infiltrated Mø and their subsets

To further summarize the dynamic changes of MG, Mø, peripheral infiltrated M1/M2 Mø, and M1/M2 MG after SCI, we integrated and analyzed the above results (Figure 2-7).

As shown in Figure 8 (first row), the proportions of total Mø/MG in the groups of sham, 1, 3, 7, 14, 21 and 28 dpi were 7%, 6%, 6%, 18%, 13%, 12% and 14%, respectively. It was suggested that the proportions in the injured spinal cords gradually increased and peaked at 7 dpi. Although the proportions decreased at 14, 21 and 28 dpi, they were still maintained at high levels compared with sham, 1 and 3 dpi groups.

The second row of Figure 8 further summarized the proportions of activated cells in total Mø/MG. We found that the proportions were 24%, 80%, 69%, 84%, 82%, 72% and 74% at sham, 1, 3, 7, 14, 21 and 28 dpi, respectively. It was suggested that most of the Mø/MG were activated following SCI.

Next, the dynamic changes of activated Mø and MG were further analyzed. As shown in row 3 of Figure 8, the proportions of activated Mø in the groups of sham, 1, 3, 7, 14, 21 and 28 dpi were 13%, 49%, 74%, 11%, 11%, 12% and 13%, respectively, and the proportions of activated MG were 87%, 51%, 26%, 89%, 89%, 88% and 87%, respectively. It can be concluded that in the sham spinal cord, MG were absolutely dominant and Mø were few. In the acute phase of SCI (1 and 3 dpi), the proportions of activated Mø increased significantly. However, with the progression of the SCI, the proportions of activated MG increased nearly to 90% in subacute phase (7 and 14 dpi) and chronic phase (21 and 28 dpi).

Finally, we further analyzed the proportion of M1 and M2 subsets in the activated MG and infiltrated Mø. As shown in row 4 of Figure 8, in sham, 1, 3, 7, 14, 21 and 28 dpi groups, the proportions of M1 Mø were 7%, 43%, 51%, 7%, 9%, 17% and 12%, respectively. The proportions of M2 Mø were 6%, 6%, 23%, 3%, 1%, 1% and 0%, respectively. The proportions of M1 MG were 31%, 43%, 20%, 69%, 79%, 66% and 68%, respectively. The proportions of M2 MG were 56%, 8%, 6%, 21%, 11%, 16% and 20%, respectively.

These results showed that there are very few peripheral Mø in the sham-operated spinal cords, and the proportion of MG is absolutely dominant, and the MG are mainly M2 subset. In the acute phase of SCI, the proportion of peripheral infiltrated Mø increased transiently, and M1 Mø are absolutely dominant, but in the subacute phase, M1 MG were absolutely dominant and continued to the chronic phase (28 dpi, the longest time point observed in this study).

Discussion

Inflammation is one of the important mechanisms of secondary pathological damage in SCI (Mallon et al. 2021). After SCI, with the destruction of blood spinal cord barrier, MG are activated, the inflammatory factors and chemokines are increased, and the peripheral immune cells infiltrate into the injured spinal cord to form an immune microenvironment, resulting in neuronal death and demyelination (Brockie et al. 2021; Rezvan et al. 2020; Shields et al. 2020). Following SCI, the different immune cell subsets with different functions affect the local immune microenvironment by producing different cytokines (Mishra et al. 2021). Previous studies have found that the local cellular components of the injured spinal cord include locally activated MG, infiltrated Mø, lymphocytes, neutrophils, dendritic cells, etc., and these cells are divided into different subsets, which have the functions of neuroprotective and neurodamaging effects (Hu et al. 2016; Ma et al. 2015; Milich et al. 2021). Moreover, neurodamaging subsets

(such as M1, Th1, Th17, etc.) are dominant, which is an important mechanism of spinal cord pathological injury (Chen et al. 2021; Chen et al. 2020). However, which of these complex immune cell populations plays a key role? So far, there is no final conclusion.

Generally, in the rodent model, the pathological process of traumatic SCI is divided into the acute (< 48 h), subacute (2 to 14 dpi) and chronic (> 14 dpi) phases (Rodrigues et al. 2018; Shi et al. 2017). Following SCI, a large number of peripheral blood-derived monocytes infiltrate into the injured spinal cord and differentiate into Mø, which are indistinguishable from the local MG, therefore the term Mø/MG was often used to define the infiltrated Mø and/or activated MG in the literatures (Fan et al. 2020; Gao et al. 2021; Rismanbaf et al. 2021). However, with the development of research methods, peripheral infiltrated Mø and locally activated MG can be identified (Chen et al. 2021; Chen et al. 2020; Milich et al. 2021). Our recent studies have found that proinflammatory M1 cells are absolutely dominant at 7 dpi following SCI, and these cells mainly from MG rather than peripheral infiltrated Mø (Chen et al. 2021; Chen et al. 2020). This suggests that M1 cells derived from MG might be the key inflammatory cells in the microenvironment of injured spinal cords. However, the dynamic patterns of MG, infiltrated Mø and their subsets during the whole pathological process of SCI are still unclear. Therefore, the purpose of this study was to explore the dynamic patterns of these cells after SCI using the strategy of combining FCM and IHF.

The results showed the proportions of total Mø/MG following SCI peaked at 7 dpi. Although the proportions decreased at 14, 21 and 28 dpi, they were still maintained at high levels comparing with sham, 1 and 3 dpi. This change trend is consistent with the previous reports of us and others (Chen et al. 2015; Kigerl et al. 2009; Wang et al. 2015). After SCI, most of the Mø/MG in the injured spinal cords was activated, especially from 7 to 28 dpi, the proportions of activated cells were the highest. The proportions of activated Mø increased significantly at 1 and 3 dpi. However, with the progression of pathological process, the proportions of activated MG increased nearly to 90% at 7, 14, 21 and 28 dpi. These demonstrate that in the early stage of SCI, the peripheral Mø infiltrate into the injured area rapidly, and the activated MG and Mø are in a roughly balanced state. This is consistent with previous report (Hellenbrand et al. 2021). However, in our report, the activated MG are dominant after 7 days. Although, this is not consistent with previous report (Hellenbrand et al. 2021), it is consistent with the recent reports which using single-cell RNA sequencing to analyze the temporal changes at molecular and cellular levels in the injured mouse spinal cords (Li et al. 2022; Milich et al. 2021). The possible reason is that MG response following acute SCI limits infiltrated Mø dispersion (Plemel et al. 2020). Accordingly, we further found that both the proportions of M1 and M2 Mø were increased significantly at 1 and 3 dpi. However, they decreased to very low levels from 7 to 28 dpi. This phenomenon also shows that the activated MG might inhibit both infiltrated M1 and M2 Mø. Following SCI, the M1 MG increased and maintained at high levels from 7 to 28 dpi. On the contrary, the proportion of M2 MG decreased significantly after SCI and remained at a low level during the whole pathological process. According to these results, we can infer that M1 cells are the main activated MG in following SCI. They inhibit not only the infiltration of peripheral monocytes, but also the polarization of these cells into M2 Mø. In the same way they can also inhibit the polarization of themselves into M2 MG. Therefore, M1 cells derived from MG are the key cells involved in proinflammatory response following SCI.

Following SCI, the main effector cells are the peripheral infiltrated Mø and resident MG (David & Kroner 2011). In fact, whether the immune response of these cells is good or bad depends on their subtypes and functional characteristics. Based on their functions, Mø/MG can be divided

into M1 and M2 subtypes. M1 cells can damage nerve cells by secreting inflammatory cytokines. M2 cells can regulate immune inflammatory response, remove necrotic tissue fragments, promote vascular regeneration, tissue reconstruction and repair (Kigerl et al. 2009; Kroner et al. 2014; Wang et al. 2015). In this study, we demonstrated that most Mø and MG in the injured spinal cords are M1 cells, only a small number showing M2 phenotype and they are transient. This shows that the predominance of M1 macroglia and lower number of M2 macroglia and/or Mø may contribute to the early inflammatory response and secondary damage following SCI. Therefore, for clinical transformation and application of Mø/MG, it is very necessary to determine the appropriate “time window” of these cells for immune intervention. Our temporal dynamic analysis suggests that the acute and early stage of subacute phase may be the "window period" for immune intervention targeting MG. In this time window, using effective intervention measures to timely inhibit the differentiation of MG into M1 type, rather than focusing on the infiltration and activation of peripheral monocytes, is of positive significance for increasing the proportion of M2 cells of injured spinal cord, improving the immune microenvironment and providing neuroprotection.

One limitation of this study is that the temporal dynamic analysis and the "window period" for immune intervention targeting MG only from mouse SCI model. Whether these laws are consistent with human related diseases still need to be further explored.

Conclusions

In summary, this study not only demonstrate that the pro-inflammatory M1 cells mainly come from MG rather than infiltrated Mø after SCI, but also determine their dynamic patterns. Therefore, these findings not only answer the academic debate about which of the infiltrating Mø and MG plays a key role, but also determines the appropriate “time window” of immune intervention targeting M1-type MG for the treatment of SCI.

Data access

The study data are available in the supplementary files

Conflicts of interest

The authors declare that they have no conflict of interests.

Financial support

This study was supported by grants from the National Natural Science Foundation of China (82072416), the 512 Talent Cultivation Plan of Bengbu Medical College (by51201109), and the high level scientific and technological innovation team fund of the First Affiliated Hospital of Bengbu Medical College (BYYFY2022TD001). He-Zuo Lü is the Principal Investigator of all the funding. The PIs are the authors of the article. The funders had no roles in the study design, conduction of experiment, data collection and analysis, decision to publish, or preparation of the manuscript.

References

Anjum A, Yazid MD, Fauzi Daud M, Idris J, Ng AMH, Selvi Naicker A, Ismail OHR, Athi Kumar RK, and Lokanathan Y. 2020. Spinal Cord Injury: Pathophysiology, Multimolecular Interactions, and Underlying Recovery Mechanisms. *Int J Mol Sci* 21. 10.3390/ijms21207533

584 Attal N. 2021. Spinal cord injury pain. *Rev Neurol (Paris)* 177:606-612.
585 10.1016/j.neurol.2020.07.003
586 Bohnert S, Seiffert A, Trella S, Bohnert M, Distel L, Ondruschka B, and Monoranu CM. 2020.
587 TMEM119 as a specific marker of microglia reaction in traumatic brain injury in
588 postmortem examination. *Int J Legal Med* 134:2167-2176. 10.1007/s00414-020-02384-z
589 Brockie S, Hong J, and Fehlings MG. 2021. The Role of Microglia in Modulating
590 Neuroinflammation after Spinal Cord Injury. *Int J Mol Sci* 22. 10.3390/ijms22189706
591 Chay W, and Kirshblum S. 2020. Predicting Outcomes After Spinal Cord Injury. *Phys Med Rehabil*
592 *Clin N Am* 31:331-343. 10.1016/j.pmr.2020.03.003
593 Chen J, Chen YQ, Shi YJ, Ding SQ, Shen L, Wang R, Wang QY, Zha C, Ding H, Hu JG, and Lu
594 HZ. 2021. VX-765 reduces neuroinflammation after spinal cord injury in mice. *Neural*
595 *Regen Res* 16:1836-1847. 10.4103/1673-5374.306096
596 Chen YJ, Zhu H, Zhang N, Shen L, Wang R, Zhou JS, Hu JG, and Lu HZ. 2015. Temporal kinetics
597 of macrophage polarization in the injured rat spinal cord. *J Neurosci Res* 93:1526-1533.
598 10.1002/jnr.23612
599 Chen YQ, Wang SN, Shi YJ, Chen J, Ding SQ, Tang J, Shen L, Wang R, Ding H, Hu JG, and Lu
600 HZ. 2020. CRID3, a blocker of apoptosis associated speck like protein containing a card,
601 ameliorates murine spinal cord injury by improving local immune microenvironment. *J*
602 *Neuroinflammation* 17:255. 10.1186/s12974-020-01937-8
603 David S, and Kroner A. 2011. Repertoire of microglial and macrophage responses after spinal
604 cord injury. *Nat Rev Neurosci* 12:388-399. 10.1038/nrn3053
605 Devanney NA, Stewart AN, and Gensel JC. 2020. Microglia and macrophage metabolism in CNS
606 injury and disease: The role of immunometabolism in neurodegeneration and
607 neurotrauma. *Exp Neurol* 329:113310. 10.1016/j.expneurol.2020.113310
608 Ding Y, Zhang D, Wang S, Zhang X, and Yang J. 2021. Hematogenous Macrophages: A New
609 Therapeutic Target for Spinal Cord Injury. *Front Cell Dev Biol* 9:767888.
610 10.3389/fcell.2021.767888
611 DiSabato DJ, Quan N, and Godbout JP. 2016. Neuroinflammation: the devil is in the details. *J*
612 *Neurochem* 139 Suppl 2:136-153. 10.1111/jnc.13607
613 Donnelly DJ, and Popovich PG. 2008. Inflammation and its role in neuroprotection, axonal
614 regeneration and functional recovery after spinal cord injury. *Exp Neurol* 209:378-388.
615 10.1016/j.expneurol.2007.06.009
616 Fan B, Wei Z, and Feng S. 2022. Progression in translational research on spinal cord injury based
617 on microenvironment imbalance. *Bone Res* 10:35. 10.1038/s41413-022-00199-9
618 Fan B, Wei Z, Yao X, Shi G, Cheng X, Zhou X, Zhou H, Ning G, Kong X, and Feng S. 2018.
619 Microenvironment Imbalance of Spinal Cord Injury. *Cell Transplant* 27:853-866.
620 10.1177/0963689718755778
621 Fan H, Tang HB, Chen Z, Wang HQ, Zhang L, Jiang Y, Li T, Yang CF, Wang XY, Li X, Wu SX,
622 and Zhang GL. 2020. Inhibiting HMGB1-RAGE axis prevents pro-inflammatory
623 macrophages/microglia polarization and affords neuroprotection after spinal cord injury. *J*
624 *Neuroinflammation* 17:295. 10.1186/s12974-020-01973-4
625 Fan H, Tang HB, Shan LQ, Liu SC, Huang DG, Chen X, Chen Z, Yang M, Yin XH, Yang H, and
626 Hao DJ. 2019. Quercetin prevents necroptosis of oligodendrocytes by inhibiting
627 macrophages/microglia polarization to M1 phenotype after spinal cord injury in rats. *J*
628 *Neuroinflammation* 16:206. 10.1186/s12974-019-1613-2
629 Gao ZS, Zhang CJ, Xia N, Tian H, Li DY, Lin JQ, Mei XF, and Wu C. 2021. Berberine-loaded M2
630 macrophage-derived exosomes for spinal cord injury therapy. *Acta Biomater* 126:211-223.
631 10.1016/j.actbio.2021.03.018
632 Greaves DR, and Gordon S. 2002. Macrophage-specific gene expression: current paradigms and
633 future challenges. *Int J Hematol* 76:6-15. 10.1007/BF02982713

Hao J, Li B, Duan HQ, Zhao CX, Zhang Y, Sun C, Pan B, Liu C, Kong XH, Yao X, and Feng SQ. 2017. Mechanisms underlying the promotion of functional recovery by deferoxamine after spinal cord injury in rats. *Neural Regen Res* 12:959-968. 10.4103/1673-5374.208591

Harrington AW, Leiner B, Blechschmitt C, Arevalo JC, Lee R, Morl K, Meyer M, Hempstead BL, Yoon SO, and Giehl KM. 2004. Secreted proNGF is a pathophysiological death-inducing ligand after adult CNS injury. *Proc Natl Acad Sci U S A* 101:6226-6230. 10.1073/pnas.0305755101

Hellenbrand DJ, Quinn CM, Piper ZJ, Morehouse CN, Fixel JA, and Hanna AS. 2021. Inflammation after spinal cord injury: a review of the critical timeline of signaling cues and cellular infiltration. *J Neuroinflammation* 18:284. 10.1186/s12974-021-02337-2

Hu JG, Shi LL, Chen YJ, Xie XM, Zhang N, Zhu AY, Jiang ZS, Feng YF, Zhang C, Xi J, and Lu HZ. 2016. Differential effects of myelin basic protein-activated Th1 and Th2 cells on the local immune microenvironment of injured spinal cord. *Exp Neurol* 277:190-201. 10.1016/j.expneurol.2016.01.002

Kigerl KA, Gensel JC, Ankeny DP, Alexander JK, Donnelly DJ, and Popovich PG. 2009. Identification of two distinct macrophage subsets with divergent effects causing either neurotoxicity or regeneration in the injured mouse spinal cord. *J Neurosci* 29:13435-13444. 10.1523/JNEUROSCI.3257-09.2009

Kilkenny C, Browne W, Cuthill IC, Emerson M, Altman DG, National Centre for the Replacement R, and Reduction of Amimals in R. 2011. Animal research: reporting in vivo experiments--the ARRIVE guidelines. *J Cereb Blood Flow Metab* 31:991-993. 10.1038/jcbfm.2010.220

Kroner A, Greenhalgh AD, Zarruk JG, Passos Dos Santos R, Gaestel M, and David S. 2014. TNF and increased intracellular iron alter macrophage polarization to a detrimental M1 phenotype in the injured spinal cord. *Neuron* 83:1098-1116. 10.1016/j.neuron.2014.07.027

Lee KD, Chow WN, Sato-Bigbee C, Graf MR, Graham RS, Colello RJ, Young HF, and Mathern BE. 2009. FTY720 reduces inflammation and promotes functional recovery after spinal cord injury. *J Neurotrauma* 26:2335-2344. 10.1089/neu.2008.0840

Li C, Wu Z, Zhou L, Shao J, Hu X, Xu W, Ren Y, Zhu X, Ge W, Zhang K, Liu J, Huang R, Yu J, Luo D, Yang X, Zhu W, Zhu R, Zheng C, Sun YE, and Cheng L. 2022. Temporal and spatial cellular and molecular pathological alterations with single-cell resolution in the adult spinal cord after injury. *Signal Transduct Target Ther* 7:65. 10.1038/s41392-022-00885-4

Ma SF, Chen YJ, Zhang JX, Shen L, Wang R, Zhou JS, Hu JG, and Lu HZ. 2015. Adoptive transfer of M2 macrophages promotes locomotor recovery in adult rats after spinal cord injury. *Brain Behav Immun* 45:157-170. 10.1016/j.bbi.2014.11.007

Mallon S, Kwiecien JM, and Karis JP. 2021. Imaging of Neurotrauma in Acute and Chronic Settings. *Curr Neuropharmacol* 19:1178-1190. 10.2174/1570159X19666210517114823

Martin E, El-Behi M, Fontaine B, and Delarasse C. 2017. Analysis of Microglia and Monocyte-derived Macrophages from the Central Nervous System by Flow Cytometry. *J Vis Exp*. 10.3791/55781

Milich LM, Choi JS, Ryan C, Cerqueira SR, Benavides S, Yahn SL, Tsoulfas P, and Lee JK. 2021. Single-cell analysis of the cellular heterogeneity and interactions in the injured mouse spinal cord. *J Exp Med* 218. 10.1084/jem.20210040

Mishra MK, Rawji KS, Keough MB, Kappen J, Dowlatabadi R, Vogel HJ, Chopra S, Distefano-Gagne F, Dufour A, Gosselin D, and Yong VW. 2021. Harnessing the Benefits of Neuroinflammation: Generation of Macrophages/Microglia with Prominent Remyelinating Properties. *J Neurosci* 41:3366-3385. 10.1523/JNEUROSCI.1948-20.2021

Perrouin-Verbe B, Lefevre C, Kieny P, Gross R, Reiss B, and Le Fort M. 2021. Spinal cord injury: A multisystem physiological impairment/dysfunction. *Rev Neurol (Paris)* 177:594-605. 10.1016/j.neurol.2021.02.385

Plemel JR, Stratton JA, Michaels NJ, Rawji KS, Zhang E, Sinha S, Baaklini CS, Dong Y, Ho M, Thorburn K, Friedman TN, Jawad S, Silva C, Caprariello AV, Hoghooghi V, Yue J, Jaffer A, Lee K, Kerr BJ, Midha R, Stys PK, Biernaskie J, and Yong VW. 2020. Microglia response following acute demyelination is heterogeneous and limits infiltrating macrophage dispersion. *Sci Adv* 6:eaay6324. 10.1126/sciadv.aay6324

Poulen G, Aloy E, Bringuier CM, Mestre-Frances N, Artus EVF, Cardoso M, Perez JC, Goze-Bac C, Boukhaddaoui H, Lonjon N, Gerber YN, and Perrin FE. 2021. Inhibiting microglia proliferation after spinal cord injury improves recovery in mice and nonhuman primates. *Theranostics* 11:8640-8659. 10.7150/thno.61833

Quadri SA, Farooqui M, Ikram A, Zafar A, Khan MA, Suriya SS, Claus CF, Fiani B, Rahman M, Ramachandran A, Armstrong IIT, Taqi MA, and Mortazavi MM. 2020. Recent update on basic mechanisms of spinal cord injury. *Neurosurg Rev* 43:425-441. 10.1007/s10143-018-1008-3

Rezvan M, Meknatkhah S, Hassannejad Z, Sharif-Alhoseini M, Zadegan SA, Shokraneh F, Vaccaro AR, Lu Y, and Rahimi-Movaghar V. 2020. Time-dependent microglia and macrophages response after traumatic spinal cord injury in rat: a systematic review. *Injury* 51:2390-2401. 10.1016/j.injury.2020.07.007

Rismanbaf A, Afshari K, Ghasemi M, Badripour A, Haj-Mirzaian A, Dehpour AR, and Shafaroodi H. 2021. Therapeutic Effects of Azithromycin on Spinal Cord Injury in Male Wistar Rats: A Role for Inflammatory Pathways. *J Neurol Surg A Cent Eur Neurosurg*. 10.1055/s-0041-1735854

Rodrigues LF, Moura-Neto V, and TCLS ES. 2018. Biomarkers in Spinal Cord Injury: from Prognosis to Treatment. *Mol Neurobiol* 55:6436-6448. 10.1007/s12035-017-0858-y

Sato A, Ohtaki H, Tsumuraya T, Song D, Ohara K, Asano M, Iwakura Y, Atsumi T, and Shioda S. 2012. Interleukin-1 participates in the classical and alternative activation of microglia/macrophages after spinal cord injury. *J Neuroinflammation* 9:65. 10.1186/1742-2094-9-65

Sedgwick JD, Ford AL, Foulcher E, and Airriess R. 1998. Central nervous system microglial cell activation and proliferation follows direct interaction with tissue-infiltrating T cell blasts. *J Immunol* 160:5320-5330.

Shi LL, Zhang N, Xie XM, Chen YJ, Wang R, Shen L, Zhou JS, Hu JG, and Lu HZ. 2017. Transcriptome profile of rat genes in injured spinal cord at different stages by RNA-sequencing. *BMC Genomics* 18:173. 10.1186/s12864-017-3532-x

Shields DC, Haque A, and Banik NL. 2020. Neuroinflammatory responses of microglia in central nervous system trauma. *J Cereb Blood Flow Metab* 40:S25-S33. 10.1177/0271678X20965786

Wang X, Cao K, Sun X, Chen Y, Duan Z, Sun L, Guo L, Bai P, Sun D, Fan J, He X, Young W, and Ren Y. 2015. Macrophages in spinal cord injury: phenotypic and functional change from exposure to myelin debris. *Glia* 63:635-651. 10.1002/glia.22774

Wolf SA, Fisher J, Bechmann I, Steiner B, Kwidzinski E, and Nitsch R. 2002. Neuroprotection by T-cells depends on their subtype and activation state. *J Neuroimmunol* 133:72-80. 10.1016/s0165-5728(02)00367-3

Zhao S, Kang R, Deng T, Luo L, Wang J, Li E, Luo J, Liu L, Wan S, and Zhao Z. 2018. Comparison of two cannulation methods for assessment of intracavernosal pressure in a rat model. *PLoS One* 13:e0193543. 10.1371/journal.pone.0193543

Figures

Figure 1 The conclusive figure that explains the pathway and the whole idea of this research.

Figure 2 Temporal pattern of MG and infiltrated Mø following SCI detected by FCM.

A: The representative pictures of FCM in sham and injured spinal cords. B-L: The temporal pattern of the indicated cell populations after SCI. The blue, red, green, purple, yellow, black and brown bars indicate sham, 1, 3, 7, 14, 21 and 28 dpi, respectively. Data represent mean ± SD (n = 6). *$P < 0.05$, **$P < 0.01$ (Non-parametric Kruskal-Wallis ANOVA, following by the individual Mann-Whitney U test).

Figure 3 Temporal pattern of MG and infiltrated Mø following SCI detected by IHF.

A-D: The representative pictures of TMEM119 (green) and CD11b (red) in the spinal cords of sham and contusion epicentre at T9 segmental level (A: sham; B: 1 dpi; C: 7 dpi; D: 28 dpi). E and F: Quantitative analysis the cells of $CD11b^+TMEM119^+$(E) and $CD11b^+TMEM119^-$(F). The blue, red, green and purple bars indicate sham, 1, 7 and 28 dpi, respectively. Data represent mean ± SD (n = 6). *$P < 0.05$, **$P < 0.01$. (Non-parametric Kruskal-Wallis ANOVA, following by the individual Mann-Whitney U test).

Figure 4 Temporal pattern of activated MG and infiltrated Mø following SCI detected by IHF.

A-D: The representative pictures of TMEM119 (green) and CD68 (red) in the spinal cords of sham and contusion epicentre at T9 segmental level (A: sham; B: 1 dpi; C: 7 dpi; D: 28 dpi). E and F: Cellular quantitation of $CD68^+TMEM119^+$(E) and $CD68^+TMEM119^-$ (F). The blue, red, green and purple bars indicate sham, 1, 7 and 28 dpi, respectively. Data represent mean ± SD (n = 6). *$P < 0.05$, **$P < 0.01$. (Non-parametric Kruskal-Wallis ANOVA, following by the individual Mann-Whitney U test).

Figure 5 Temporal pattern of SCI-induced M1 and M2 differentiation of Mø and MG detected by FCM.

A, E and I: Representative images of total M1 and M2 cells (A), M1 and M2 MG (E), M1 and M2 Mø (I) detected by FCM in sham and injured spinal cords. B-D, F-H and J-L: The temporal pattern of the indicated cell populations after SCI. The blue, red, green, purple, yellow, black and brown bars indicate sham, 1, 3, 7, 14, 21 and 28 dpi, respectively. Data represent mean ± SD (n = 6). *$P < 0.05$, **$P < 0.01$. (Non-parametric Kruskal-Wallis ANOVA, following by the individual Mann-Whitney U test).

Figure 6 Temporal pattern of SCI-induced differentiation of total M1 and M2 cells following SCI detected by IHF.

A-H: The representative pictures of CCR7 (green) and CD68 (red) (A-D), and Arg1 (green) and CD68 (red) (E-H) in the spinal cords of sham and contusion epicentre at T9 segmental level (A, E: sham; B, F: 1 dpi; C, G: 7 dpi; D, H: 28 dpi). I and J: Cellular quantitation of $CD68^+CCR7^+$(I) and $CD68^+Arg1^+$(J). The blue, red, green and purple bars indicate sham, 1, 7 and 28 dpi, respectively. Data represent mean ± SD (n = 6). *$P < 0.05$, **$P < 0.01$. (Non-parametric Kruskal-Wallis ANOVA, following by the individual Mann-Whitney U test).

Figure 7 Temporal pattern of SCI-induced M1 and M2 differentiation of Mø and MG following SCI detected by IHF.

A-H: The representative pictures of CCR7 (green) and TMEM119 (red) (A-D), and Arg1 (green) and TMEM119 (red) (E-H) in the spinal cords of sham and contusion epicentre at T9 segmental level (A, E: sham; B, F: 1 dpi; C, G: 7 dpi; D, H: 28 dpi). I-L: Cellular quantitation of $TMEM119^{+}CCR7^{+}$ (I), $TMEM119^{+}Arg1^{+}$ (J) cells, infiltrated M1 Mø (K) and infiltrated M1 Mø (L). The blue, red, green and purple bars indicate sham, 1, 7 and 28 dpi, respectively. Data represent mean ± SD (n = 6). $*P < 0.05$, $**P < 0.01$. (Non-parametric Kruskal-Wallis ANOVA, following by the individual Mann-Whitney U test).

Figure 8 Summary of dynamic changes of MG, infiltrated Mø and their subsets.

This is an integrated analysis of the above results (Figure 2-7). The purpose is to summarize the dynamic changes of MG, infiltrated Mø and their subsets. The first to seventh lines indicate sham, 1, 3, 7, 14, 21 and 28 dpi, respectively. The first row shows the proportions of total Mø/MG (red) and the other cells (green). The second row shows the proportions of activated (light green) and resting (brown) cells in total Mø/MG. The third row shows the proportions of activated Mø (blue) and activated MG (yellow) in the activated Mø/MG. The fourth row shows the proportion of M1 and M2 subsets in the activated MG and infiltrated Mø (dark blue: M1 Mø; light blue: M2 Mø; dark yellow: M1 MG; light yellow: M2 MG).

Tables

Table 1 Antibodies used in the study

Figure 1

The conclusive figure that explains the pathway and the whole idea of this research

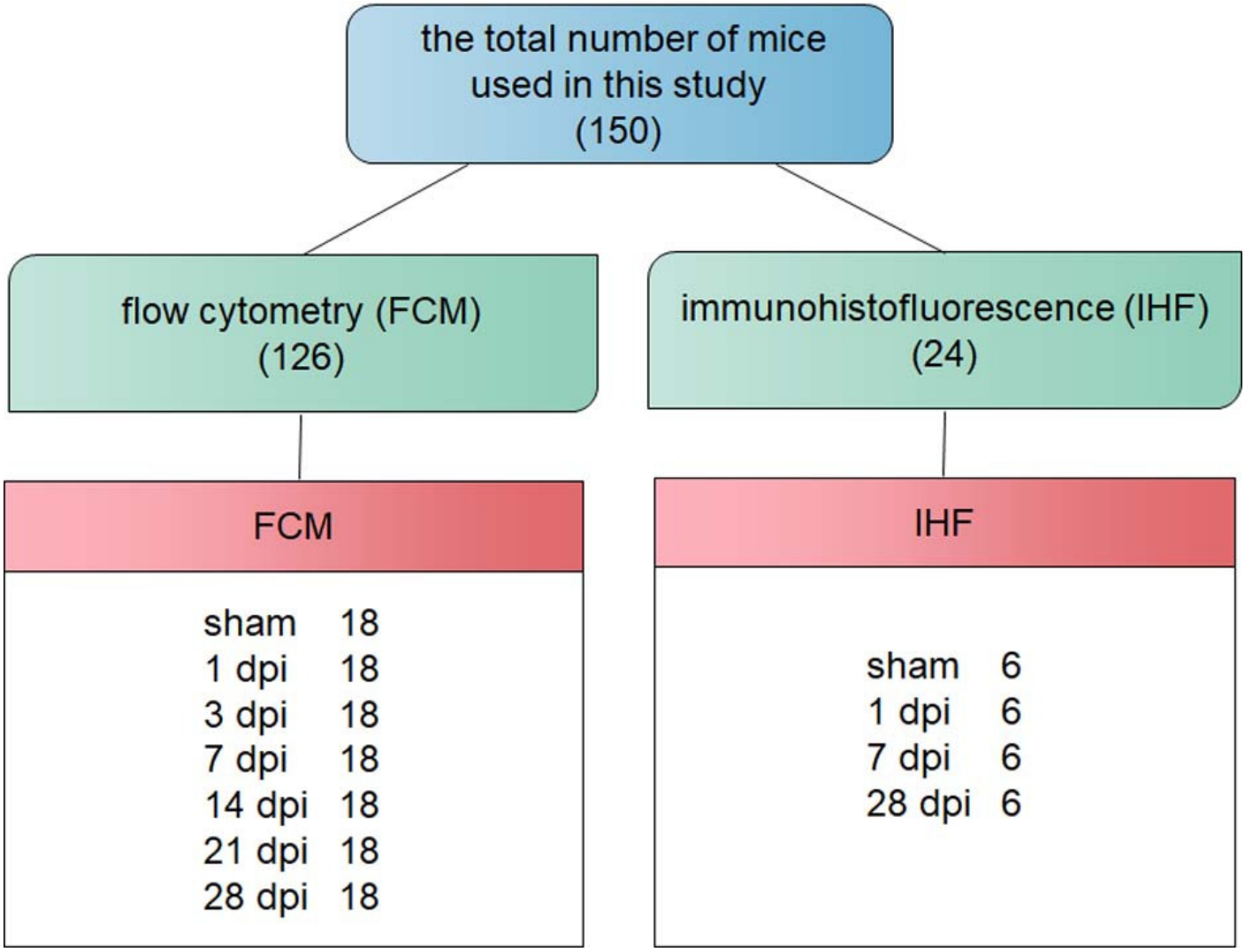

Figure 2

Temporal pattern of MG and infiltrated Mø following SCI detected by FCM

A: The representative pictures of FCM in sham and injured spinal cords. B-L: The temporal pattern of the indicated cell populations after SCI. The blue, red, green, purple, yellow, black and brown bars indicate sham, 1, 3, 7, 14, 21 and 28 dpi, respectively. Data represent mean ± SD (n = 6). *$P < 0.05$, **$P < 0.01$ (Non-parametric Kruskal-Wallis ANOVA, following by the individual Mann-Whitney U test).

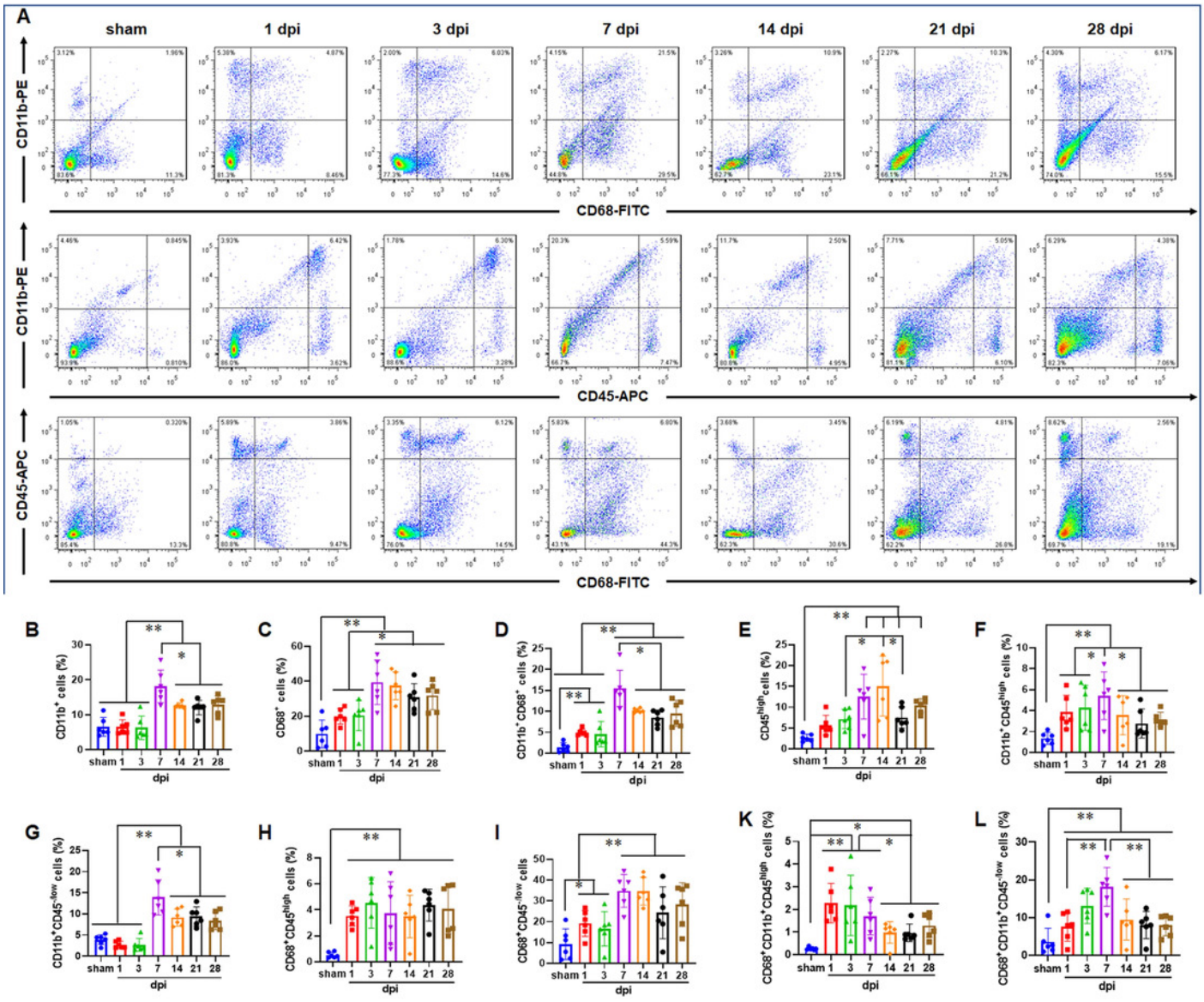

Figure 3

Temporal pattern of MG and infiltrated Mø following SCI detected by IHF

A-D: The representative pictures of TMEM119 (green) and CD11b (red) in the spinal cords of sham and contusion epicentre at T9 segmental level (A: sham; B: 1 dpi; C: 7 dpi; D: 28 dpi). E and F: Quantitative analysis the cells of $CD11b^{+}TMEM119^{+}$(E) and $CD11b^{+}TMEM119^{-}$(F). The blue, red, green and purple bars indicate sham, 1, 7 and 28 dpi, respectively. Data represent mean ± SD (n = 6). $*P < 0.05$, $**P < 0.01$. (Non-parametric Kruskal-Wallis ANOVA, following by the individual Mann-Whitney U test).

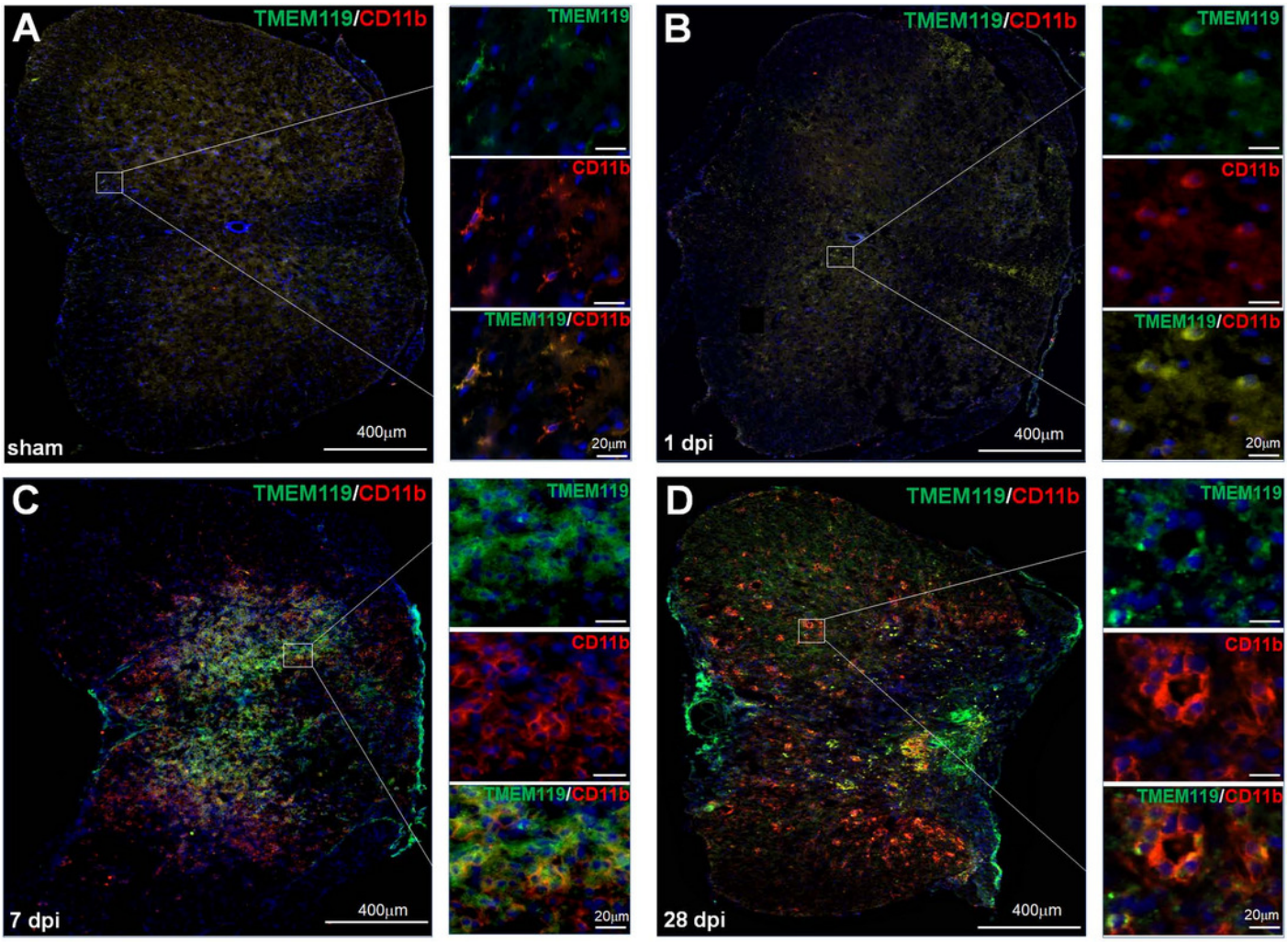
A
TMEM119/CD11b
TMEM119
CD11b
TMEM119/CD11b
sham
400μm
20μm
B
1 dpi
C
7 dpi
D
28 dpi

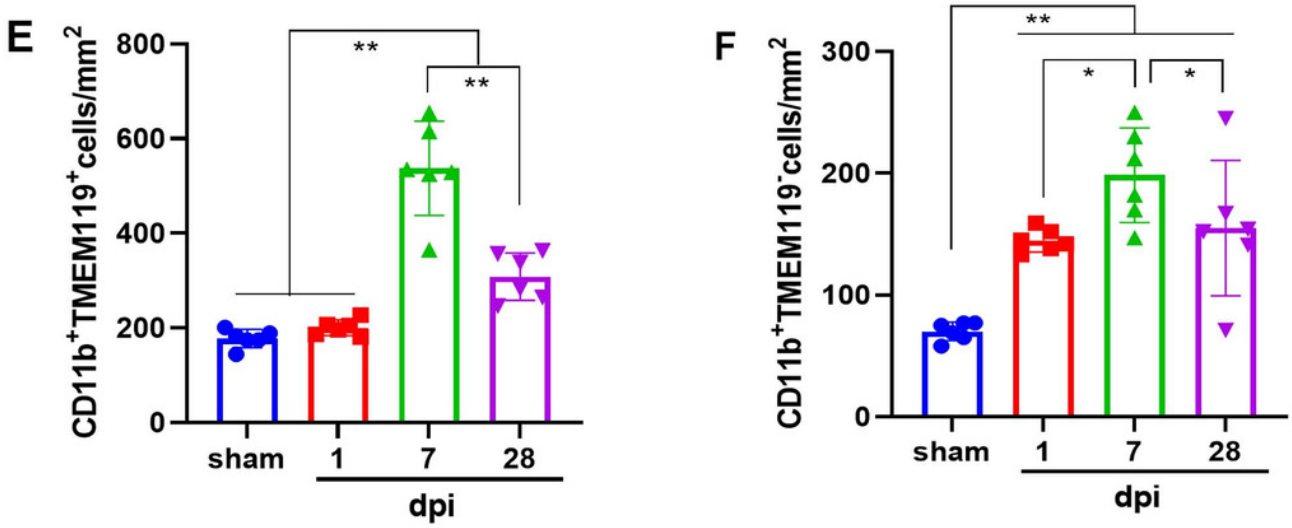
E
CD11b+TMEM119+cells/mm2
800
600
400
200
0
**
**
sham
1
7
28
dpi
F
CD11b+TMEM119-cells/mm2
300
200
100
0
**
*
*

Figure 4

Temporal pattern of activated MG and infiltrated Mø following SCI detected by IHF

A-D: The representative pictures of TMEM119 (green) and CD68 (red) in the spinal cords of sham and contusion epicentre at T9 segmental level (A: sham; B: 1 dpi; C: 7 dpi; D: 28 dpi). E and F: Cellular quantitation of $CD68^{+}TMEM119^{+}$(E) and $CD68^{+}TMEM119^{-}$ (F). The blue, red, green and purple bars indicate sham, 1, 7 and 28 dpi, respectively. Data represent mean ± SD (n = 6). *$P < 0.05$, **$P < 0.01$. (Non-parametric Kruskal-Wallis ANOVA, following by the individual Mann-Whitney U test)

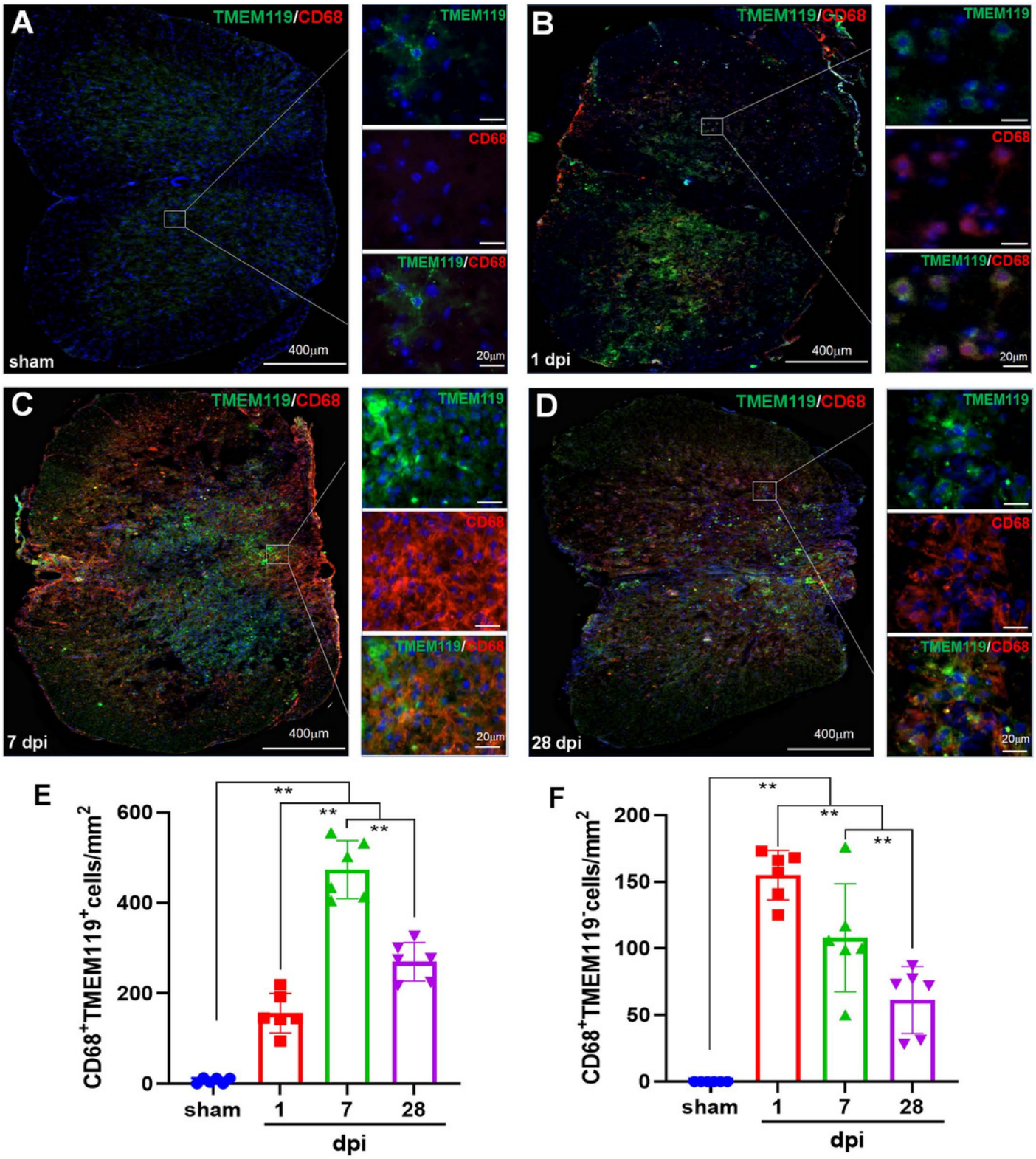
A
TMEM119/CD68
TMEM119
CD68
TMEM119/CD68
sham
400μm
20μm
B
1 dpi
C
7 dpi
D
28 dpi
E
CD68+TMEM119+cells/mm2
600
400
200
0
**
sham
1
7
28
dpi
F
CD68+TMEM119-cells/mm2
200
150
100
50

Figure 5

Temporal pattern of SCI-induced M1 and M2 differentiation of Mø and MG detected by FCM

A, E and I: Representative images of total M1 and M2 cells (A), M1 and M2 MG (E), M1 and M2 Mø (I) detected by FCM in sham and injured spinal cords. B-D, F-H and J-L: The temporal pattern of the indicated cell populations after SCI. The blue, red, green, purple, yellow, black and brown bars indicate sham, 1, 3, 7, 14, 21 and 28 dpi, respectively. Data represent mean ± SD (n = 6). $*P < 0.05$, $**P < 0.01$. (Non-parametric Kruskal-Wallis ANOVA, following by the individual Mann-Whitney U test).

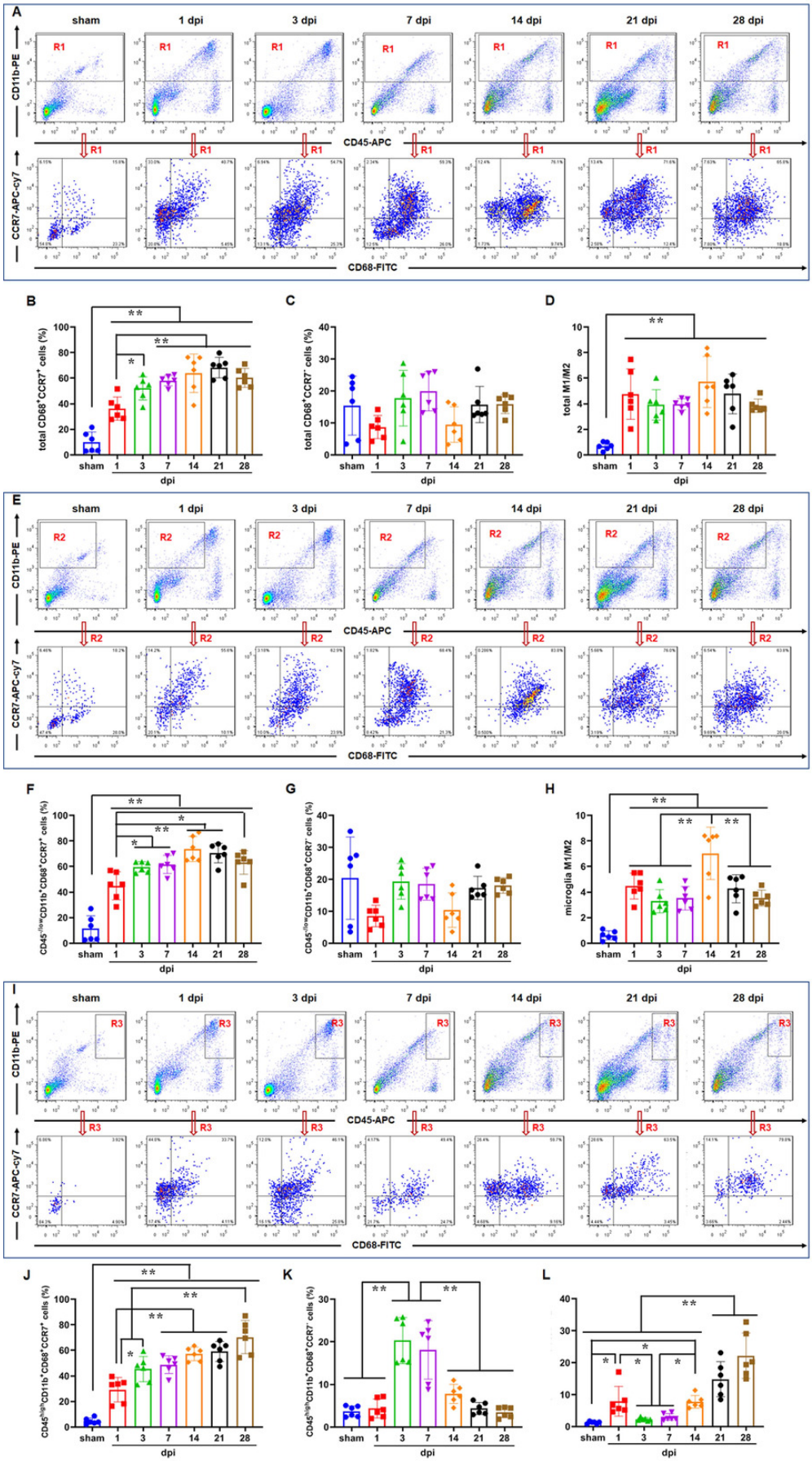
A
sham
1 dpi
3 dpi
7 dpi
14 dpi
21 dpi
28 dpi
CD11b-PE
CD45-APC
CCR7-APC-cy7
CD68-FITC
R1
B
total CD68+CCR7+ cells (%)
C
total CD68+CCR7- cells (%)
D
total M1/M2
dpi
E
R2
F
CD45low CD11b+CD68+CCR7+ cells (%)
G
CD45low CD11b+CD68+CCR7- cells (%)
H
microglia M1/M2
I
R3
J
CD45high CD11b+CD68+CCR7+ cells (%)
K
CD45high CD11b+CD68+CCR7- cells (%)
L

Figure 6

Temporal pattern of SCI-induced differentiation of total M1 and M2 cells following SCI detected by IHF

A-H: The representative pictures of CCR7 (green) and CD68 (red) (A-D), and Arg1 (green) and CD68 (red) (E-H) in the spinal cords of sham and contusion epicentre at T9 segmental level (A, E: sham; B, F: 1 dpi; C, G: 7 dpi; D, H: 28 dpi). I and J: Cellular quantitation of $CD68^{+}CCR7^{+}$(I) and $CD68^{+}Arg1^{+}$(J). The blue, red, green and purple bars indicate sham, 1, 7 and 28 dpi, respectively. Data represent mean ± SD (n = 6). $*P < 0.05$, $**P < 0.01$. (Non-parametric Kruskal-Wallis ANOVA, following by the individual Mann-Whitney U test).

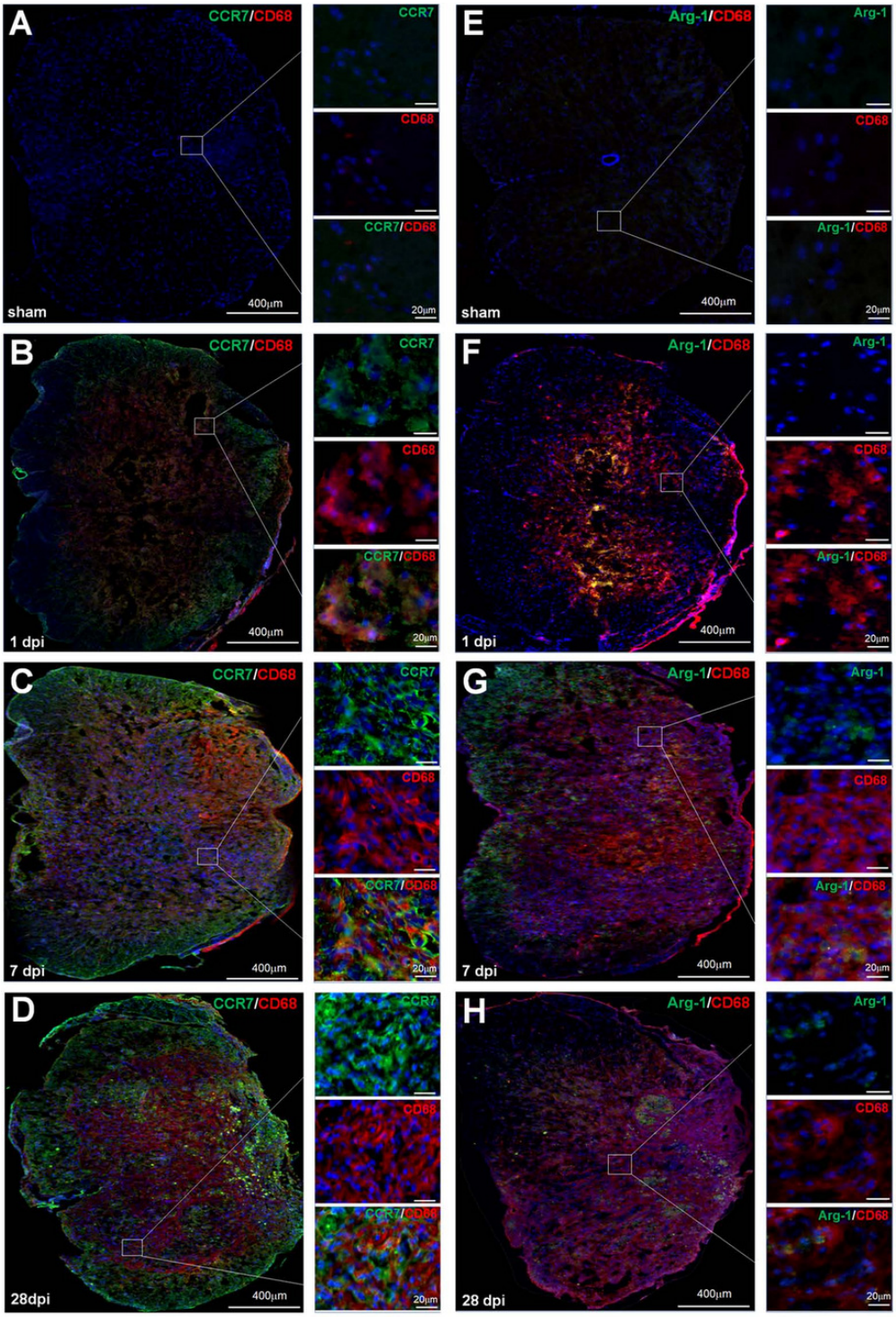
A
CCR7/CD68
CCR7
CD68
CCR7/CD68
sham
400μm
20μm
E
Arg-1/CD68
Arg-1
CD68
Arg-1/CD68
B
1 dpi
F
C
7 dpi
G
D
28dpi
H
28 dpi

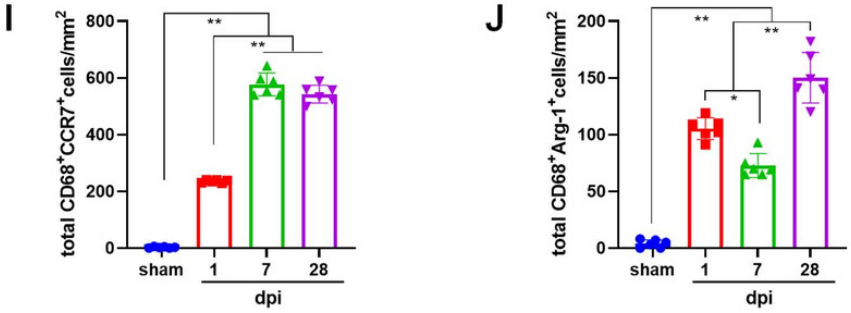
I
total CD68+CCR7+cells/mm2
800
600
400
200
0
**
**
sham
1
7
28
dpi
J
total CD68+Arg-1+cells/mm2
200
150
100
50
0
**
**
*

Figure 7

Temporal pattern of SCI-induced M1 and M2 differentiation of Mø and MG following SCI detected by IHF

A-H: The representative pictures of CCR7 (green) and TMEM119 (red) (A-D) , and Arg1 (green) and TMEM119 (red) (E-H) in the spinal cords of sham and contusion epicentre at T9 segmental level (A, E: sham; B, F: 1 dpi; C, G: 7 dpi; D, H: 28 dpi). I-L: Cellular quantitation of $TMEM119^{+}CCR7^{+}$ (I), $TMEM119^{+}Arg1^{+}$ (J) cells, infiltrated M1 Mø (K) and infiltrated M1 Mø (L). The blue, red, green and purple bars indicate sham, 1, 7 and 28 dpi, respectively. Data represent mean ± SD (n = 6). $*P < 0.05$, $**P < 0.01$. (Non-parametric Kruskal-Wallis ANOVA, following by the individual Mann-Whitney U test).

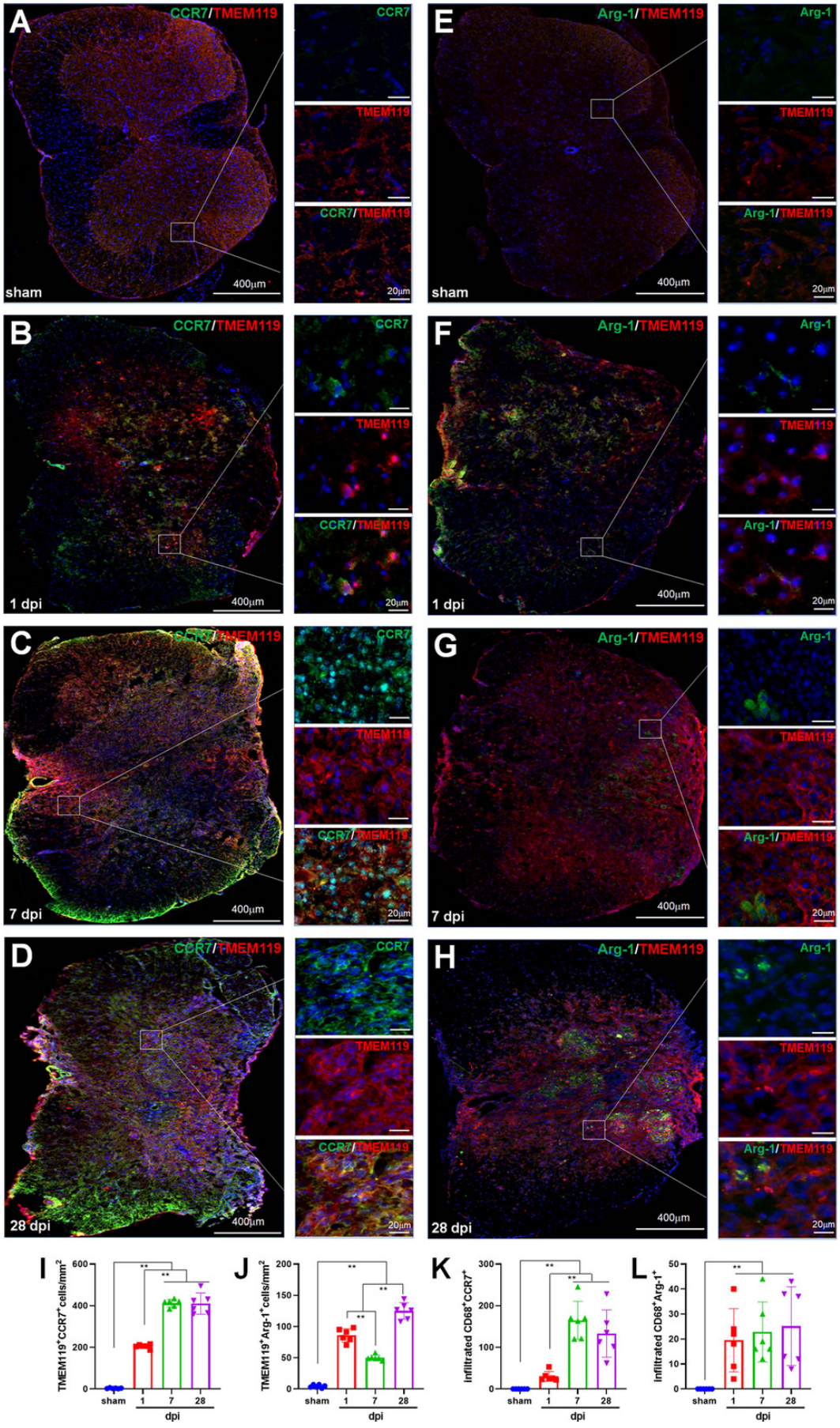
A
CCR7/TMEM119
CCR7
TMEM119
CCR7/TMEM119
sham
400μm
20μm
E
Arg-1/TMEM119
Arg-1
TMEM119
Arg-1/TMEM119
B
1 dpi
F
C
7 dpi
G
D
28 dpi
H
I
TMEM119+CCR7+cells/mm2
J
TMEM119+Arg-1+cells/mm2
K
Infiltrated CD68+CCR7+
L
Infiltrated CD68+Arg-1+
dpi

Figure 8

Summary of dynamic changes of MG, infiltrated Mø and their subsets

This is an integrated analysis of the above results (Figure 2-7). The purpose is to summarize the dynamic changes of MG, infiltrated Mø and their subsets. The first to seventh lines indicate sham, 1, 3, 7, 14, 21 and 28 dpi, respectively. The first row shows the proportions of total Mø/MG (red) and the other cells (green). The second row shows the proportions of activated (light green) and resting (brown) cells in total Mø/MG. The third row shows the proportions of activated Mø (blue) and activated MG (yellow) in the activated Mø/MG. The fourth row shows the proportion of M1 and M2 subsets in the activated MG and infiltrated Mø (dark blue: M1 Mø; light blue: M2 Mø; dark yellow: M1 MG; light yellow: M2 MG).

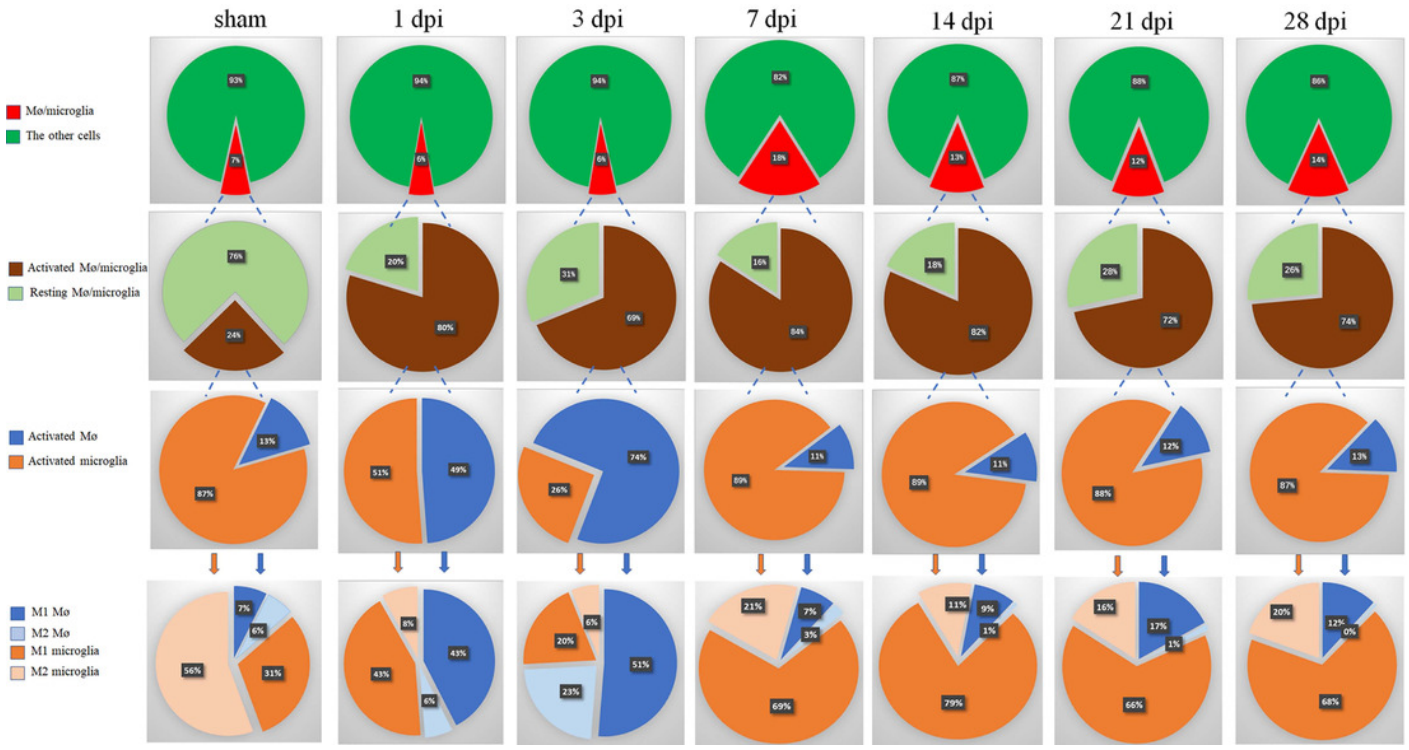

Table 1(on next page)

Antibodies used in the study

Antibodies used in the study

1 **Table 1 Antibodies used in the study**

2

Antigen	Host Species and Clone	Cat. # or Lot#	RRID	Conjugation	Source	Used concentration	Methods
CD11b	rat monoclonal	14-0112-82	AB_467108	NO	Invitrogen	1:200	IHF
CD45	rat monoclonal	14-0451-82	AB_467251				
CD68	rat monoclonal	MA5-16674	AB_2538168				
Arg1	rabbit polyclonal	PA5-29645	AB_2547120				
CCR7	rabbit polyclonal	ab191575			Abcam		
TMEM119	rat monoclonal	ab209064	AB_2800343				
Rat IgG (H+L)	goat polyclonal	112-095-143	AB_2338199	Fluorescein (FITC)	Jackson ImmunoResearch		
Rabbit IgG (H+L)	goat polyclonal	111-025-144	AB_2337932	Rhodamine (TRITC)			
CCR7	rat monoclonal	47-1971-82	AB_2573974	APC-eFluor 780 (AF780)	Invitrogen	0.25 μg/test	FCM
IgG2b kappa Isotype Control	rat	47-4321-82	AB_1271997				
CD11b	rat monoclonal	12-0112-81	AB_465546	PE		0.125 μg/test	
IgG2b kappa Isotype	rat	12-4031-82	AB_470042			0.25 μg/test	

Control							
CD68	rat monoclonal	MA5-16676	AB_2538170	FITC			
IgG2b kappa Isotype Control	rat	11-4031-82	AB_470004				
CD45	rat monoclonal	17-0451-82	AB_469392	APC		0.125 µg/test	
IgG2b kappa Isotype Control	rat	17-4031-82	AB_470176				

3